

Research Project

Progress Towards a Gravitational Constant Value from Light Deflections by Solar System Objects

Zhaobo Wang

24068000

University College London

Dissertation submitted for the degree of
MSc Scientific and Data Intensive Computing

Supervisor: Prof. Jonathan Tennyson

Acting Supervisor: Dr. Tony Lynas-Gray

August 21, 2025



I, Zhaobo Wang, confirm that the work presented in this dissertation is my own. Where information has been derived from other sources, I confirm that this has been indicated in the dissertation.

Link of the Github repository:

GitHub Repository

https://github.com/w93185205/PHAS0077_ZHAOBO_WANG.git

Abstract

This dissertation investigates the influence of gravitational light deflection by Solar System bodies on the precision of astrometric measurements with the Square Kilometre Array (SKA), and explores its potential role in refining the determination of the gravitational constant G . Within the framework of general relativity, a numerical model was developed to calculate maximum deflection angles for 59 major Solar System objects, including the Sun, planets, moons, and selected asteroids, alongside a systematic uncertainty analysis.

The results show that the Sun produces the dominant effect, with a maximum deflection of about $1.75 \times 10^6 \mu\text{as}$. Jupiter and Saturn follow with deflections of $1.66 \times 10^4 \mu\text{as}$ and $5.98 \times 10^3 \mu\text{as}$, respectively, both well within the expected sensitivity of SKA astrometry. Earth and Venus produce deflections of several hundred μas , while the Moon and large satellites such as Ganymede reach tens of μas , making their contributions non-negligible.

Furthermore, extend the analysis to the dual-planet scenario by introducing a methodology for modeling simultaneous light deflections from two planetary bodies. Numerical experiments based on linear superposition demonstrate that such combined effects, though subtle, can accumulate to levels significant for future high-precision astrometric observations.

In conclusion, this study demonstrates that multi-body light deflection within the Solar System must be systematically modelled in SKA data analysis pipelines. Doing so will not only ensure microarcsecond-level accuracy in astrometric measurements but also provide a novel astronomical pathway toward improving the determination of the gravitational constant G .

Acknowledgements

I would like to express my heartfelt gratitude to Dr. Tony Lynas-Gray, for his patient guidance and encouragement throughout this project. As a student without a strong background in physics, I often struggled with concepts and ideas, yet he always took the time to explain them with great care and kindness. His support not only helped me complete this work, but also gave me confidence to keep moving forward.

I am also deeply grateful to Prof. Jonathan Tennyson for his valuable advice when I was choosing my project, and for his insightful suggestions on my dissertation writing. His guidance helped me present my work in a clearer and more thoughtful way.

I would also like to thank Jiahao Geng, whose dissertation provided me with inspiration and valuable reference throughout the progress of my own work.

My sincere thanks go to UCL for providing such excellent resources and to all the staff who dedicate their efforts to the university and its students. Without this supportive environment, my studies would not have been possible.

I owe my deepest appreciation to my parents, who supported me in coming alone to the UK to study and encouraged me in every choice I made. It is because I stand on their shoulders that I am able to see a wider world.

Finally, I would like to thank myself for having the courage to make the decision to study at UCL. This past year has been a truly special journey, I have grown so much and experienced a broader and more wonderful world than I could have imagined.

Contents

Contents	i
List of Figures	iii
List of Tables	v
1 Introduction	1
1.1 Background	1
1.1.1 Gravitational Light Deflection	1
1.1.2 Measurement of the Gravitational Constant G	1
1.1.3 Square Kilometer Array (SKA) and high-precision astrometry	2
1.1.4 Established research	2
1.2 Objectives and Motivation	2
1.2.1 Research Objectives	2
1.2.2 Research Motivation	3
1.3 Outline of the Dissertation	3
2 Literature Review	4
2.1 Fundamentals of the Theory of Light Deflection and Gravity	4
2.2 Classical Observations and Historical Progress	5
2.3 Gravitational Effect of Solar System Bodies	5
2.4 Uncertainty in Gravitational Constant G and Astronomical Measurements .	6
2.5 SKA and High-Precision Astronomical Measurements	6
2.6 Multicelestial Body Gravitational Modelling and Analysis of Deflection Effects	7
2.7 Jet Propulsion Laboratory (JPL) and DE440s	8
2.8 Gravitational Impact Rating in Measurements	8
3 Methodology	9
3.1 Dataset Classification and Organization	9
3.1.1 Dataset Overview	9

3.1.2 Principles of Classification of Celestial Bodies	9
3.1.3 Data Sources and Parameters	10
3.1.4 Data Processing and Consistency	10
3.1.5 Data Storage and Structuring	10
3.1.6 Data Visualization and Validation	11
3.2 Determining Planetary and CES Positions	12
3.2.1 Planetary Positions from Ephemerides	12
3.2.2 Constructing CES Positions	12
3.3 Impact Parameter Calculation	13
3.3.1 Geometrical Definition of the Impact Parameter	13
3.3.2 Vector Definition, Projection, and Impact Parameter ¹²	14
3.4 Gravitational Deflection of Light	16
3.4.1 Deflection at Small Distances ($b \approx R$) ²³	16
3.4.2 Deflection at Large Distances ($b \gg R$) ²³	16
3.4.3 Criteria for Deflection Analysis	17
3.5 Synodic Period Determination	17
3.6 Method to Compute the Impact Range	17
3.7 Dual Planet Light Deflection	19
3.7.1 Geometry and Notation	19
3.7.2 Single Body Deflection and Dual Body Superposition	20
4 Results and Analysis	21
4.1 Impact of Uncertainties in the Gravitational Constant G and Planetary Masses	21
4.2 The Deflection Angle α	22
4.3 Impact Ranges	25
4.4 Differentiation Based Analysis of $\alpha(\beta)$ and the Impact Ranges	31
4.4.1 Geometry to Deflection	31
4.4.2 Implicit Differentiation of β	31
4.4.3 Endpoint Expansions	32
4.5 Perturbation Duration of Light Deflection	33
4.6 Dual-Planet Linear Superposition Results	35
5 Conclusion and Future Work	38
5.1 Conclusion	38
5.2 Limitation	39
5.3 Future Work	39
Bibliography	41

List of Figures

3.1	Data visualization and validation: (left) Kepler's Third Law verification using a logarithmic scatter plot of semi-major axis and orbital period; (right) example of parameter uncertainty for Mars.	11
3.2	Reference frame centered at the SSB with planetary position vectors and scaled CES distance.	13
3.3	Geometrical definition of the impact parameter b , shown as the perpendicular distance from the deflecting body P to the unperturbed light path CE . P' is the projection of P onto the light path.	14
3.4	Extended observer-to-source and planet vectors. The grey line indicates the light path \vec{EC} , the blue arrow marks \vec{EP} from the observer to the deflecting body, the purple point P' is the projection onto the light ray, and the dashed black line corresponds to the impact parameter $b = \ \vec{P} - \vec{P}'\ $	15
3.5	Configuration with $\beta < 90^\circ$. The observer E , lens L , and source C define the geometry. The undeflected path is shown as a dotted line and the deflected trajectory as a dashed line. The impact parameter b is measured perpendicular to the undeflected ray. Angles θ_1 and θ_0 describe the photon direction with respect to the lens near E and near C , respectively. ²	16
3.6	Configuration with $\beta > 90^\circ$. Same notation as Fig. 3.5. The layout emphasizes the case where the observer to lens to source angle exceeds 90° , which changes the relative orientation of the asymptotes that define α . ²	17
3.7	Flowchart of the calculation process.	18
3.8	Geometry and notation for the dual-planet case: line of sight $\hat{\ell}$ from E to C ; planet directions $r_i \hat{p}_i$; angles β_i and impact parameters b_i ; projected tangent directions t_i and unit vectors \hat{n}_i	19
4.1	Maximum gravitational deflection (logarithmic scale) for Solar System bodies.	23
4.2	Threshold maps (I): Saturn and Jupiter. Left: r_{\max} ; Right: r_{\min}	28
4.3	Threshold maps (II): Venus and Uranus. Left: r_{\max} ; Right: r_{\min}	29
4.4	Threshold maps (III): Neptune, Mercury, and Mars. Left: r_{\max} ; Right: r_{\min} .	30

4.5	Jupiter consistency check (Cartesian, semi-log y). Pale vertical bands: half-span implied by this work, $\Delta\beta/2 \approx 5.29^\circ$ from $\tau_{10} = 23.453$ days, which lies within the model bracket, demonstrating consistency.	34
4.6	Jupiter–Saturn components vs total. The total deflection almost coincides with Jupiter’s curve, with a nearly constant fractional uplift due to Saturn across β	36
4.7	Uranus–Neptune components vs total. The total closely follows the algebraic sum because the two single-body contributions are comparable across β . . .	37

List of Tables

2.1	Values of the gravitational constant G and their relative standard uncertainties.	6
2.2	Key Technical Parameters of SKA1-Low and SKA1-Mid	7
2.3	Gravitational influence levels of Solar System bodies on SKA astrometry . .	8
4.1	Relative uncertainties of GM for the eight planets under different correlation assumptions.	22
4.3	Comparison of gravitational light deflection angles (μas) for 59 Solar System bodies. Columns show the adopted mass and radius, the results of this study, and reference values from Geng (2023) and Li et al. (2022).	25
4.4	Impact angle β in degrees at three thresholds. Superscripts 10, 1, and 0.1 denote 10 μas , 1 μas , and 0.1 μas , respectively.	26
4.5	Perturbation duration of major Solar–System bodies at different deflection thresholds (days).	33
4.6	Jupiter–Saturn wide table (units: μas).	35
4.7	Jupiter-Saturn and Uranus-Neptune linear superposition table (units: μas). .	35

Chapter 1

Introduction

1.1 Background

1.1.1 Gravitational Light Deflection

Gravitational light deflection is one of the earliest verified fundamental predictions of general relativity. According to Einstein's theory, massive celestial bodies induce curvature in the surrounding space-time, thereby altering the path of light rays.³ This effect was first confirmed experimentally during the observation of a total solar eclipse in 1919, the measurement results at that time were highly consistent with the theoretical predictions of general relativity, which provided a strong empirical support for the theory.⁴

Over the course of more than a century of subsequent observations, research into light deflection has continued to develop. From early measurements of arcsecond-level deflections caused by the Sun to modern radio interferometry (VLBI) capable of detecting weak deflections at the microarcsecond level.⁵ Although the deflection effect of the Sun is most significant, planets, satellites, and even asteroids can also cause measurable deflection of light passing near them. Therefore, in the era of high-precision astrometry, these effects must be incorporated into theoretical models.

1.1.2 Measurement of the Gravitational Constant G

Among the fundamental physical constants in nature, Newton's gravitational constant G is known for its large measurement uncertainty. Measurements from different laboratories often show differences that exceed the experimental error range. In contrast, physical constants such as the speed of light and Planck's constant have been measured accurately to more than ten significant digits.⁶ However, the relative uncertainty of G remains at the level of 10^{-5} . In theoretical calculations of gravitational light deflection, G appears directly in the relevant

formulas, thus the uncertainty in its value will be directly reflected in the predicted deflection angle, this is one of the key factors limiting the accuracy of high-precision gravitational tests and astrometry.⁷

1.1.3 Square Kilometer Array (SKA) and high-precision astrometry

The Square Kilometre Array (SKA) is one of the largest and most ambitious radio astronomy projects currently underway worldwide.⁷ The design goals of SKA include achieving astronomical measurement accuracy at the sub-microarcsecond level and extremely high observational sensitivity.⁸ This enables direct measurement of not only the gravitational light deflection caused by the Sun, but also minute deflection effects caused by planets, satellites, and even asteroids are expected to be observed.

To make full use of this capacity, all relevant relativistic corrections must be introduced precisely in the data processing flow. If these effects are ignored, systematic errors may be introduced in the measurement of celestial positions, thereby affecting the results of a number of scientific studies, including tests of gravitational theory.

1.1.4 Established research

Li et al. (2022) systematically predicted the maximum gravitational light deflection effect for 195 Solar System bodies, covering the Sun, planets, major satellites and some asteroids.³ The spatial distribution range and temporal variation characteristics of the deflection effect are also given, and these results provide important theoretical references for high-precision astrometry. However, existing studies have not yet systematically analysed the impact of uncertainty in G on the prediction results, although the bias effect has been calculated with high precision. Therefore, the feasibility of inverting G by observing light deflection with high accuracy remains to be further explored.

1.2 Objectives and Motivation

1.2.1 Research Objectives

The main goal of this study is to reproduce and extend the prediction of gravitational light deflection for Solar System objects within the theoretical framework proposed by Li et al. (2022). Introducing the measurement uncertainty of the gravitational constant G into the calculations and assessing its range of influence on the predictions. In addition, this study aims to analyse the feasibility of using high-precision astrometry to invert G , and focus on

the future observational potential of the Square Kilometre Array (SKA).²

Specific objectives of this study include: reproducing and validating predictions of maximum light deflections for major Solar System objects, to ensure numerical consistency of the calculation methodology with published data. Introducing the measurement error of the gravitational constant G in the deflection calculation and quantitatively assessing its impact on the prediction accuracy. Exploring the inversion of G using high-precision light deflection observations.

1.2.2 Research Motivation

The motivation for this study is to explore new ways to accurately determine the underlying physical constants using astronomical methods.

As a central prediction of general relativity, gravitational light deflection is not only an important physical phenomenon for testing the theory of gravity, but also constitutes a key link between astrometry and the measurement of the gravitational constant G .⁴ With the development of high-precision astrometric techniques, in particular the unprecedented observational capabilities offered by the Square Kilometre Array (SKA), tiny light deflections induced by planets and small Solar System objects are expected to be directly detected. This provides a unique opportunity to independently constrain G through astronomical observations, not only does it help to improve the accuracy of light deflection studies, but also offers new solutions to alleviate the long-standing problem of measurement discrepancies in G .

1.3 Outline of the Dissertation

The remainder of this dissertation is structured as follows. Chapter 2 reviews the relevant literature on gravitational light deflection, measurement of G , and the capabilities of the SKA. Chapter 3 describes the methodology, including data preparation, impact parameter calculation, and the dual-planet deflection framework. Chapter 4 presents the numerical results and analysis, covering single-body and dual-planet cases. Finally, Chapter 5 provides the conclusions, limitations, and directions for future work.

Chapter 2

Literature Review

2.1 Fundamentals of the Theory of Light Deflection and Gravity

The deflection of light in a gravitational field was one of the first important predictions of general relativity to be confirmed experimentally.⁹ According to Einstein's theory, gravity is the bending of space-time caused by mass, light travels out of alignment when passing near massive objects.¹⁰ In the weak-field approximation, the deflection angle for a spherically symmetric mass M can be expressed as³

$$\delta\theta = \frac{4GM}{c^2b} \quad (2.1)$$

where G is the gravitational constant, b is the impact parameter, and c is the speed of light. This relationship not only reveals the direct connection between light deflection and G , but also lays a theoretical foundation for the inversion of G based on astronomical observation.

The observation of a total solar eclipse in 1919 was the first verification of the light deflection effect, and the result was in high agreement with Einstein's prediction.¹¹ Subsequently, researchers extended the theory to account for scenarios involving the frame-dragging effect of rotating bodies, non-spherical mass distributions, and higher-order relativistic corrections, which significantly improved model accuracy.¹² In recent years, advances in high-precision radio astronomy techniques such as Very Long Baseline Interferometry (VLBI) have enabled light-deflection studies to simultaneously account for the gravitational perturbations of multiple Solar System bodies.¹³

2.2 Classical Observations and Historical Progress

Experimental verification of the effect of light deflection dates back to observations made by Eddington's team during a total solar eclipse in 1919, they measured the amount of deflection of stellar light in the Sun's gravitational field in agreement with the theoretical predictions of general relativity.¹⁴ This becomes an important experimental support for Einstein's theory.¹¹ This result has not only sparked widespread interest in the physics community, but also marks the first time that astronomical observations have directly tested the effect of gravity on the path of light propagation.¹⁵

In the decades since then, the means of observation have undergone an evolution from optical imaging to radio interferometry. The development of very long baseline interferometry (VLBI) in the mid-twentieth century dramatically improved angular resolution and measurement accuracy, which enables verification of optical deflection effects in different wavelength bands and with higher precision.^{13 16} During this period, researchers not only repeatedly verified the light deflection effect of the Sun's gravity, but also began to explore the gravitational bending of other Solar System bodies such as planets and moons.¹⁷

In the twenty-first century, the observational focus shifted from single-body deflections to multi-body scenarios, analysed in conjunction with precise planetary ephemerides and relativistic light propagation models.³ These advances have allowed astronomers to more accurately separate the contributions of different celestial gravitational fields, which lays the observational foundation for the application of light deflection in the measurement of fundamental physical constants and the testing of gravitational theories.

2.3 Gravitational Effect of Solar System Bodies

In addition to the Sun, the gravitational fields of planets, satellites and some asteroids also cause measurable light deflection in high-precision astronomical observations.³ The magnitude of the deflection is directly proportional to the mass of the object and inversely proportional to the distance the light has travelled.¹⁰ Thus the effects of massive planets such as Jupiter and Saturn can be on the order of milliarcseconds, and the effects of asteroids and large satellites cannot be ignored at micro-angle second accuracy.⁵

Multi-planet gravitational effects are more complex in their temporal and spatial distribution, which require accurate celestial calendars and propagation models for predictions.¹⁸ If these deflections are ignored, systematic errors will be introduced in high-precision observations,

thereby affecting positional measurements and scientific conclusions.¹⁷

2.4 Uncertainty in Gravitational Constant G and Astronomical Measurements

The gravitational constant G is the central parameter in Newton's law of gravity, but it has the lowest measurement accuracy of all the fundamental physical constants.¹⁹ Independent measurements from different laboratories often differ significantly, bias is often greater than the uncertainty of the respective experiments.^{6 19} In contrast, the relative uncertainties of the speed of light c and the Planck constant h have already reached levels better than 10^{-9} , whereas that of G remains at the order of 10^{-5} .¹⁹

Since the gravitational deflection prediction of light is proportional to G , uncertainty in G directly affects the accuracy of modeling deflection effects in astronomical observations. The following table gives the CODATA-recommended values for all previous G measurements.²⁰

Year	G ($\text{m}^3 \cdot \text{kg}^{-1} \cdot \text{s}^{-2}$)	Relative uncertainty
1986	6.67259×10^{-11}	1.2×10^{-4}
2006	6.67428×10^{-11}	1.0×10^{-4}
2010	6.67384×10^{-11}	1.2×10^{-4}
2018	6.67430×10^{-11}	2.2×10^{-5}

Table 2.1: Values of the gravitational constant G and their relative standard uncertainties.

In recent years, methods for inferring G through high-precision astronomical observations, such as Very Long Baseline Interferometry (VLBI) and the Square Kilometre Array (SKA), have attracted increasing attention.²⁰ Unlike laboratory measurements, these methods allow independent measurements in large-scale gravitational fields, helping to verify the consistency of G in different physical environments.

2.5 SKA and High-Precision Astronomical Measurements

The Square Kilometre Array (SKA) is the world's largest radio telescope programme, divided into SKA1-Low in Australia and SKA1-Mid in South Africa, both cover a wide band from tens of megahertz to thousands of megahertz.^{8 21} Its large effective receiving area and long-baseline VLBI capability provide angular resolution down to the microarcsecond level, provide unprecedented precision for the study of light deflection by celestial bodies in

the Solar System.¹³

The high sensitivity of the SKA significantly increases the number of available background radio sources for optical deflection measurements.²² Li et al. (2022) showed that SKA can monitor planet-induced weak deflection effects over large samples and long timescales, and test the theory of gravity in conjunction with the planetary calendar.³ Thus, SKA will not only drive the development of high-precision astronomical measurements, but will also play a key role in fundamental physics testing.

To visually demonstrate the advantages of SKA in observation capabilities, Table 2.2 summarizes the main technical parameter comparisons between SKA1-Low and SKA1-Mid.²¹

Parameter	SKA1-Low (Australia)	SKA1-Mid (South Africa)
Observing frequency range	50–350 MHz	0.35–15.3 GHz
Maximum baseline length	65 km	150 km (extendable to global VLBI)
Angular resolution (VLBI)	≈ 0.2'' @ 350 MHz	≈ 0.02'' @ 1.4 GHz
Instantaneous bandwidth	up to 300 MHz	up to 5 GHz
Sensitivity improvement (over current facilities)	≈ 10×	≈ 5–10×

Table 2.2: Key Technical Parameters of SKA1-Low and SKA1-Mid

2.6 Multicelestial Body Gravitational Modelling and Analysis of Deflection Effects

In high-precision astronomical measurements, a superimposed deflection effect occurs when light passes through the gravitational fields of multiple bodies in the Solar System. Most of the traditional modelling of light deflection is based on the single-body approximation, i.e., the deflection angles of individual celestial bodies, such as the Sun, planets, etc., are calculated separately and then linearly superimposed.²³ However, as the observational accuracy is improved to the microarcsecond level, this approach requires the introduction of relativistic corrections, higher order ingress terms, and time-dependent corrections due to celestial motion.³ The general form of the total deflection angle of a multicelestial body can be written as:²³

$$\Delta\theta_{\text{total}} \approx \sum_{i=1}^N \frac{4GM_i}{c^2b_i} \cdot f_i(v_i, r_i, t) \quad (2.2)$$

where M_i denotes the mass of the i -th body, b_i is the impact parameter between the incoming light ray and the body, and f_i is a correction factor that accounts for the velocity v_i , position

\mathbf{r}_i , and time t of the body.¹² This expression can be used flexibly to consider the combined effect of massive objects on the propagation path of light under different observational geometries.

It has been shown that with the observational accuracy of the SKA, the deflection of Jupiter at solar transits can be in the order of hundreds of microarcseconds, and the contribution of Saturn and Uranus in specific geometrical configurations should not be overlooked.² Therefore, when inverting the gravitational constant G using light deflection or performing precision astrometry, it is necessary to use multicelestial body relativistic modelling.

2.7 Jet Propulsion Laboratory (JPL) and DE440s

The DE series of ephemerides released by NASA's Jet Propulsion Laboratory (JPL) are widely used for space navigation and high-precision astronomical research.²⁴ DE440s.bsp is a compact version of the DE440 series, covering the years 1849-2150, optimised for calculating the positions of planets and major bodies in the Solar System Barycentre of Mass (SSB) reference system, with small file size and high accuracy.²⁵ In this study, the planetary positions and velocities provided by DE440s are used to calculate the impact parameter b_i and to correct for relativistic effects due to celestial motion.²⁶

2.8 Gravitational Impact Rating in Measurements

Gravitational light deflection effects of the Solar System objects need to be classified and managed according to their degree of influence in the Square Kilometre Array (SKA) microarcsecond high-precision astronomical measurements. For modelling and error control purposes, the influence of celestial gravity is usually classified into the following five classes according to the amount of deflection:²³

Influence Level	Deflection Range (α)
Negligible	$\alpha < 0.01 \mu\text{as}$
Minor	$0.01 \mu\text{as} < \alpha < 0.1 \mu\text{as}$
Moderate	$0.1 \mu\text{as} < \alpha < 1 \mu\text{as}$
Significant	$1 \mu\text{as} < \alpha < 10 \mu\text{as}$
Severe	$\alpha > 10 \mu\text{as}$

Table 2.3: Gravitational influence levels of Solar System bodies on SKA astrometry

Chapter 3

Methodology

3.1 Dataset Classification and Organization

3.1.1 Dataset Overview

In this study, a dataset covering 59 major Solar System objects is constructed with the aim of providing reliable input data to support gravitational deflection calculations.² The data objects were chosen not only for their mass and size, but also in conjunction with their scientific significance in gravitational physics research.

3.1.2 Principles of Classification of Celestial Bodies

Based on the physical characteristics of celestial bodies and the significance of their gravitational effects, the selected targets are classified into the following categories.

Sun: Representative body: Sun. It is the strongest gravitational source and the main contributor to light deflection.

Planets: Representative bodies include Mercury, Venus, Earth, Mars, Jupiter, and Saturn (covering the eight major planets). These objects have complete and well determined orbital and mass data.

Dwarf planet: Representative body: Pluto. Although reclassified as a dwarf planet, it remains important in gravitational studies.

Moons: Representative bodies include Io and Earth's Moon. These relatively massive natural satellites can produce significant gravitational effects on light propagation.

Asteroids: Representative bodies include Ceres, Vesta, and Pallas. These large asteroids, many of which follow orbits close to that of Earth, are also considered in the analysis.

3.1.3 Data Sources and Parameters

All parameters are primarily obtained from the NASA JPL Horizons system, with orbital data based on the DE440s ephemeris, ensuring scientific reliability.

The core physical and orbital parameters collected include:

- **Mass (M)**: Used for calculating gravitational strength.
- **Radius (R)**: Determines the impact parameter.
- **Orbital elements**: Semi-major axis, eccentricity, inclination, and mean motion.

3.1.4 Data Processing and Consistency

All celestial body parameters in this study are obtained from the **DE440s** ephemeris. To ensure comparability and consistency in subsequent gravitational deflection calculations, the following steps were applied:²⁴

Unit Standardization

All physical quantities were converted to the International System of Units (SI): mass in kilograms (kg), length in kilometers (km), and time in seconds (s).³

Precision Verification

After processing, the difference between processed and original values at the same epoch was evaluated using the relative error:

$$\delta = \frac{|X_{\text{processed}} - X_{\text{original}}|}{X_{\text{original}}} \times 100\% \quad (3.1)$$

All key parameters were confirmed to have $\delta < 10^{-6}$, ensuring numerical precision.

3.1.5 Data Storage and Structuring

The raw data were first archived in CSV format for long-term preservation and readability. During numerical computation, the data were converted into NumPy arrays to significantly improve processing efficiency.¹

Each celestial body was organized in a dictionary-like data structure, for example:

```
planet_data = {
    "Mercury": {"mass": 3.3011e23, "radius": 2439.7, "semi_axis": 5.791e7},
    "Venus": {"mass": 4.8675e24, "radius": 6051.8, "semi_axis": 1.082e8}
}
```

This structure ensures that each celestial body's physical and orbital parameters are stored in a consistent and easily accessible format, facilitating efficient retrieval and computation in subsequent analysis.

3.1.6 Data Visualization and Validation

To assess the accuracy and physical consistency of the dataset, two types of visualizations were produced, as shown in Figure 3.1.

1. Orbital Law Verification

Based on Kepler's Third Law:

$$T^2 \propto a^3 \quad (3.2)$$

a logarithmic scatter plot of the semi-major axis a versus orbital period T for the planets was drawn, with the theoretical relation line overlaid. For accurate data, the points should align closely with the theoretical line.²⁷ This visualization provides a direct check of consistency with theory and helps identify any anomalies in orbital parameters.

2. Parameter Uncertainty

Using Mars as an example, an error bar plot was drawn for its mass and semi-major axis, where the horizontal and vertical error bars represent the observational uncertainty ranges of each parameter. This visualization helps to evaluate the potential impact of measurement uncertainties on gravitational deflection calculations.

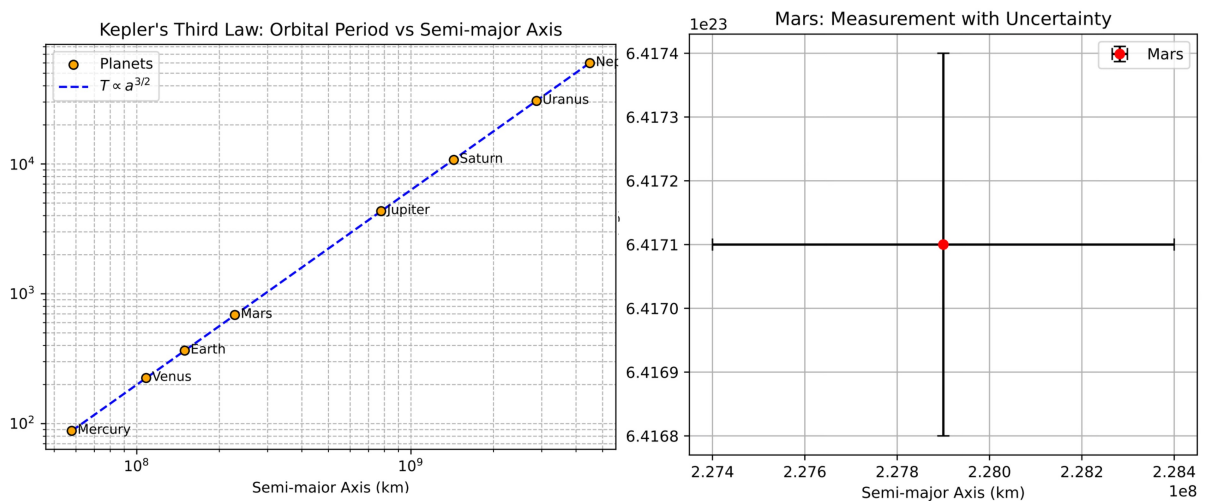


Figure 3.1: Data visualization and validation: (left) Kepler's Third Law verification using a logarithmic scatter plot of semi-major axis and orbital period; (right) example of parameter uncertainty for Mars.

3.2 Determining Planetary and CES Positions

In order to simulate the process of gravitational deflection of light rays by multiple bodies in the Solar System, it is necessary to accurately obtain the spatial positions of planets relative to the Solar System Barycenter (SSB).² The observational geometry of the Compact Extragalactic Sources (CES) is constructed from these positions. In this study, position calculations were performed under the unified Barycentric Celestial Reference System (BCRS).

3.2.1 Planetary Positions from Ephemerides

For a given epoch t , the three-dimensional position vector of a planet with respect to the Solar System Barycenter (SSB) is expressed as¹

$$\vec{r}_{\text{Planet}}(t) = \text{Ephemeris}(t) \quad (3.3)$$

where *Ephemeris* refers to the planetary orbital data provided by the JPL DE440s ephemeris file.²⁸ The vector is represented in Cartesian coordinates, with units in kilometers (km).

3.2.2 Constructing CES Positions

In the model, Compact Extragalactic Sources (CES) are used to simulate distant radio sources for analyzing gravitational deflection effects. To ensure that each CES shares the same line of sight as its corresponding planet, the CES position vector is defined to be in the same direction as the planetary position vector, scaled by a constant factor M :¹

$$\vec{r}_{\text{CES}}(t) = M \cdot \vec{r}_{\text{Planet}}(t) \quad (3.4)$$

In this study, $M = 10^6$ is adopted so that the CES is placed at a distance much greater than the Solar System scale, effectively eliminating parallax effects:

$$\frac{\|\vec{r}_{\text{Planet}}(t)\|}{\|\vec{r}_{\text{CES}}(t)\|} \approx 10^{-6} \ll 1 \quad (3.5)$$

This configuration simplifies subsequent deflection angle calculations by treating CES light as parallel rays from infinity, while maintaining high physical realism in the simulated geometry.

The following figure illustrates the reference frame centered at the Solar System Barycenter (SSB). On the left, the three-dimensional coordinate system shows the instantaneous position vectors $\vec{r}_{\text{Earth}}(t)$, $\vec{r}_{\text{Mars}}(t)$, and $\vec{r}_{\text{Saturn}}(t)$ from the SSB to Earth, Mars, and Saturn, respectively. On the right, the schematic indicates the scale relationship, where the distance from

the SSB to a planet is set to 1 unit, while the distance from the SSB to the far-field reference point CES is 10^6 units, highlighting the vast difference in spatial scale between planetary positions and the celestial reference direction.

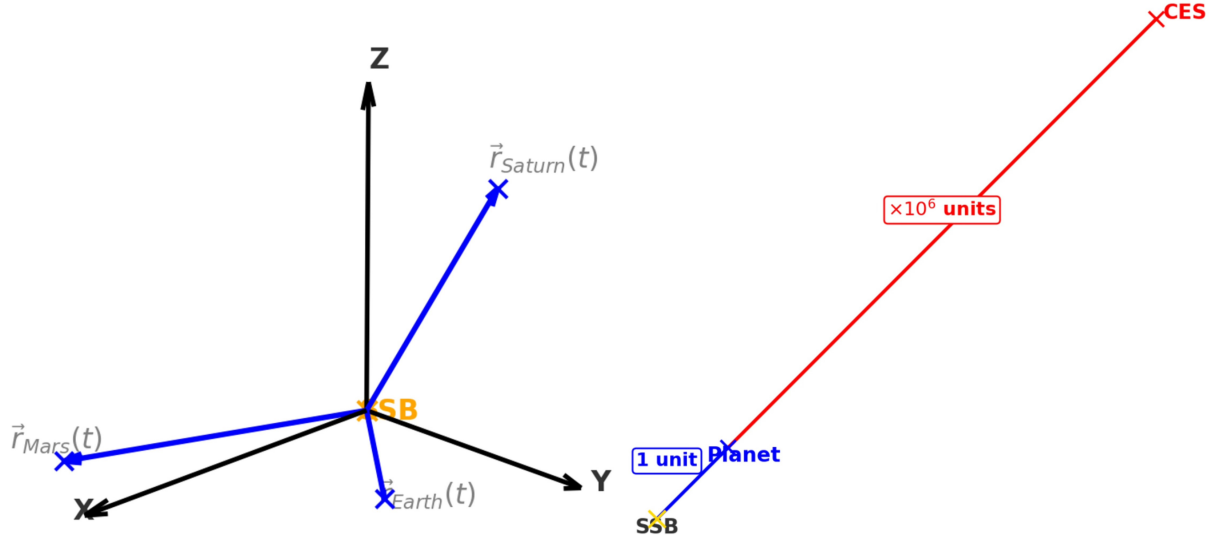


Figure 3.2: Reference frame centered at the SSB with planetary position vectors and scaled CES distance.

3.3 Impact Parameter Calculation

3.3.1 Geometrical Definition of the Impact Parameter

In gravitational light deflection theory, the *impact parameter* b describes the relative position between the light ray and the deflecting body.²³ It is defined as the **shortest distance** between the unperturbed light path and the centre of mass of the deflecting body. In the general relativity deflection formula, b appears in the denominator, and its magnitude directly influences the size of the deflection angle.¹²

As illustrated in Figure 3.3, the observer (Earth) is denoted by E , the deflecting celestial body by P , and the compact extragalactic source (CES) by C . Without gravitational deflection, the light path is a straight line from C to E . Project P perpendicularly onto this light path, and denote the projection point by P' . The length of the segment PP' is then the impact parameter:

$$b = \|\overrightarrow{PP'}\|, \quad (3.6)$$

where PP' is perpendicular to the light path CE . In subsequent calculations, b will serve as a key input for determining the amount of light deflection.

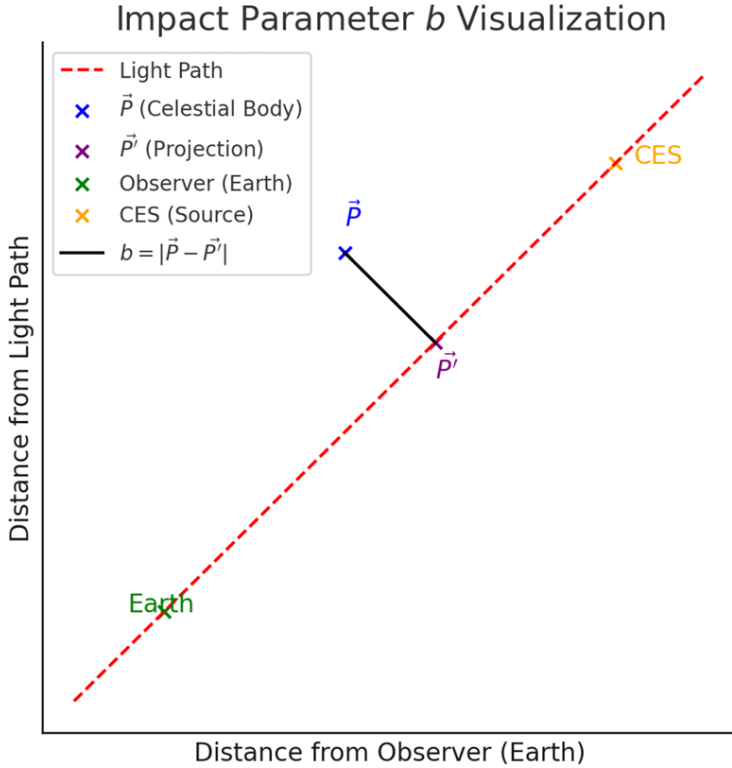


Figure 3.3: Geometrical definition of the impact parameter b , shown as the perpendicular distance from the deflecting body P to the unperturbed light path CE . P' is the projection of P onto the light path.

3.3.2 Vector Definition, Projection, and Impact Parameter¹²

In order to characterise the spatial configuration between the incoming light ray and the deflecting body, first establish a set of vectors in the barycentric reference frame. Let \vec{E} denote the position vector of the observer (Earth), and \vec{C} the position vector of the Compact Extragalactic Source (CES). The unit vector that specifies the direction of the undeflected light ray from the observer to the source is defined as

$$\vec{EC} = \frac{\vec{C} - \vec{E}}{\|\vec{C} - \vec{E}\|}. \quad (3.7)$$

This expression removes the dependence on the physical separation between E and C , retaining only the propagation direction.

Similarly, the location of the deflecting body relative to the observer is represented by

$$\vec{EP} = \vec{P} - \vec{E}, \quad (3.8)$$

where \vec{P} denotes the barycentric position vector of the body at the time of observation.¹

To identify the point on the light path that lies closest to the deflecting body, we compute the orthogonal projection of \vec{EP} onto the direction of \vec{EC} . The projection length, measured from the observer along the light ray, is

$$s = \frac{\vec{EC} \cdot \vec{EP}}{\|\vec{EC}\|}. \quad (3.9)$$

The coordinates of the projected point P' on the light path then follow as¹

$$\vec{P}' = \vec{E} + s \vec{EC} = \vec{E} + \frac{\vec{EC} \cdot \vec{EP}}{\|\vec{EC}\|^2} \vec{EC}. \quad (3.10)$$

This ensures that P' lies exactly along the straight line connecting E and C .

The impact parameter b is the shortest distance between the deflecting body and the light path, and can be written in vector form as¹

$$b = \|\vec{P} - \vec{P}'\| = \left\| \vec{EP} - \frac{\vec{EC} \cdot \vec{EP}}{\|\vec{EC}\|^2} \vec{EC} \right\|. \quad (3.11)$$

The above framework provides a direct way to determine b from the known barycentric positions of the observer, the source, and the deflecting body without requiring any intermediate transformations.

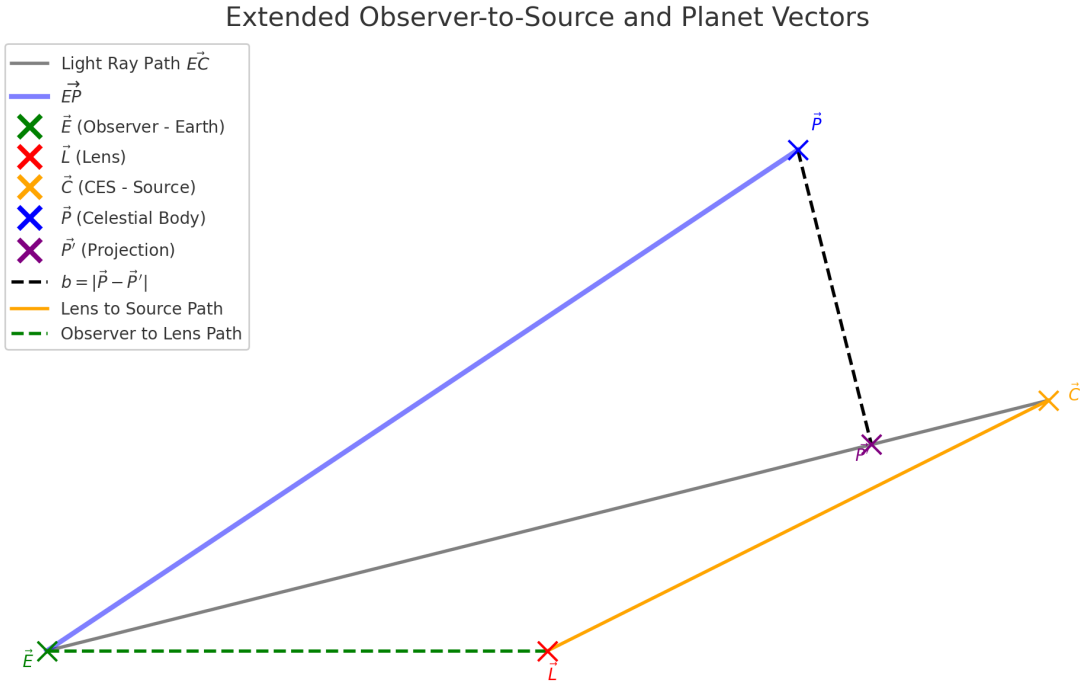


Figure 3.4: Extended observer-to-source and planet vectors. The grey line indicates the light path \vec{EC} , the blue arrow marks \vec{EP} from the observer to the deflecting body, the purple point P' is the projection onto the light ray, and the dashed black line corresponds to the impact parameter $b = \|\vec{P} - \vec{P}'\|$.

3.4 Gravitational Deflection of Light

When a photon passes through the curved spacetime generated by a massive body, its trajectory is bent. The deflection angle α is governed primarily by two elements: the closest approach of the light ray to the mass, quantified by the impact parameter b , and the gravitational potential of the deflector.²⁹ The angle β denotes the angle between the observer to source direction and the observer to lens vector.³

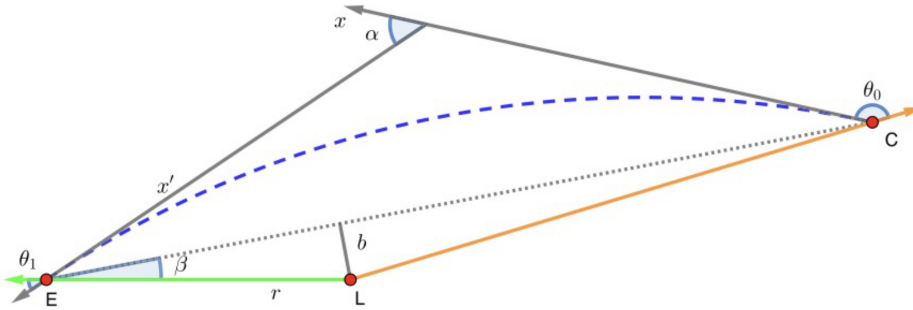


Figure 3.5: Configuration with $\beta < 90^\circ$. The observer E , lens L , and source C define the geometry. The undeflected path is shown as a dotted line and the deflected trajectory as a dashed line. The impact parameter b is measured perpendicular to the undeflected ray. Angles θ_1 and θ_0 describe the photon direction with respect to the lens near E and near C , respectively.²

3.4.1 Deflection at Small Distances ($b \approx R$)²³

If the incoming photon passes very close to the surface of the body, the deflection angle can be written as

$$\alpha = (1 + \gamma) \frac{GM}{c^2 b} (\cos \theta_1 - \cos \theta_0), \quad (3.12)$$

where γ is the post Newtonian parameter, which equals 1 in General Relativity. The angles θ_1 and θ_0 encode the geometric configuration of the photon path with respect to the deflector.

3.4.2 Deflection at Large Distances ($b \gg R$)²³

For trajectories that remain far from the deflecting body, higher order contributions can be neglected and the expression reduces to

$$\alpha = (1 + \gamma) \frac{2GM}{c^2 b}. \quad (3.13)$$

This approximation holds when the photon passes at a distance far greater than the body's radius, ensuring that the gravitational effect remains relatively weak.

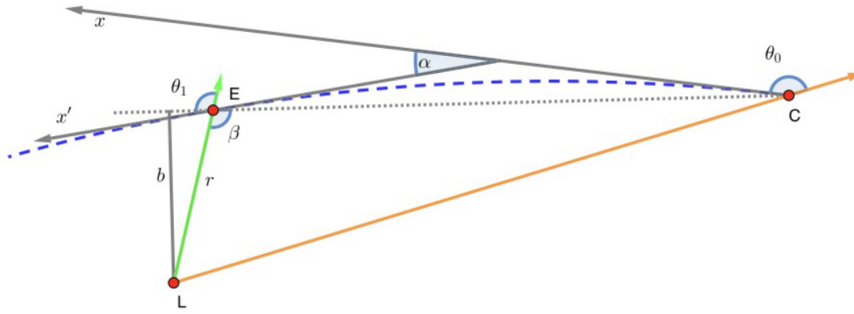


Figure 3.6: Configuration with $\beta > 90^\circ$. Same notation as Fig. 3.5. The layout emphasizes the case where the observer to lens to source angle exceeds 90° , which changes the relative orientation of the asymptotes that define α .²

3.4.3 Criteria for Deflection Analysis

To assess when gravitational bending is significant for astrometric work, I adopt threshold angles that delineate regimes of interest:^{1,2}

$$\alpha > 0.1 \mu\text{as}, \quad 1.0 \mu\text{as}, \quad 10.0 \mu\text{as}.$$

These thresholds provide a practical way to map regions where light deflection must be modeled to maintain microarcsecond level precision.

3.5 Synodic Period Determination

The synodic period P_{syn} represents the time interval after which Earth and another planet realign to the same relative position with respect to the Sun.²

It depends on the sidereal orbital periods of Earth (P_{\oplus}) and the planet (P_p), and is determined by the relative angular velocities of the two bodies.³⁰

For inferior planets ($P_p < P_{\oplus}$), the synodic period is given by:

$$P_{\text{syn}} = \frac{1}{\frac{1}{P_p} - \frac{1}{P_{\oplus}}}. \quad (3.14)$$

For superior planets ($P_p > P_{\oplus}$), the formula becomes:

$$P_{\text{syn}} = \frac{1}{\frac{1}{P_{\oplus}} - \frac{1}{P_p}}. \quad (3.15)$$

3.6 Method to Compute the Impact Range

To evaluate the influence of Solar System bodies on high-precision astrometry, I compute their *impact ranges*, defined as the angular separations within which the light deflection

exceeds a given accuracy threshold.

The calculation is based on the General Relativity deflection formula, with the following assumptions:

1. The observed source is a distant compact extragalactic object with incident angle $\theta_0 = 180^\circ$.
2. The post-Newtonian parameter is set to $\gamma = 1$.
3. At the $0.1 \mu\text{as}$ level, the angle β can be approximated as θ_1 .³

The impact parameter is

$$b = r \sin \beta, \quad (3.16)$$

with r the Earth–body distance. The corresponding deflection angle is

$$\alpha(\beta) = \frac{2GM}{c^2 r \sin \beta} (\cos \beta + 1), \quad (3.17)$$

where M is the body mass, G the gravitational constant, and c the speed of light.

For each object, both minimum and maximum distances between Earth and bodies are considered:

- Sun: $r = 1 \text{ AU}$.
- Others: $r_{\min} = |R_{\text{au}} - 1| \times \text{AU}$, $r_{\max} = (R_{\text{au}} + 1) \times \text{AU}$.

The workflow is implemented in Python: given the body mass, distance, and accuracy thresholds (10, 1, and $0.1 \mu\text{as}$), the equation $f(\beta) = \alpha(\beta) - \alpha_{\text{th}}$ is solved numerically using `root_scalar` to obtain β_{\min} and β_{\max} . The solutions are converted into degrees and arcseconds, providing impact ranges for each body that indicate the angular regions where their influence must be corrected in precise astrometric measurements.

The flowchart of the workflow is summarized below:

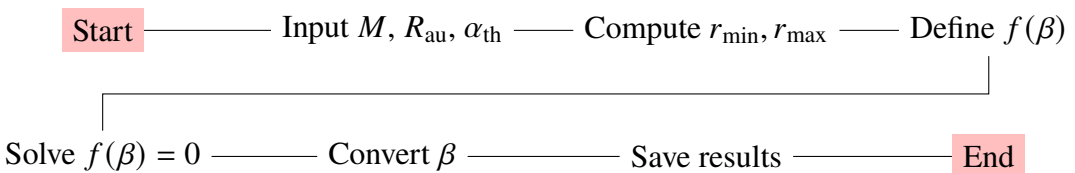


Figure 3.7: Flowchart of the calculation process.

3.7 Dual Planet Light Deflection

In realistic astrometric observations the line of sight to a distant compact source often passes through regions where more than one Solar System body contributes to the gravitational bending. We refer to this as the *dual planet problem*. Unlike the single body case, the deflection is a two dimensional vector in the sky tangent plane and depends not only on the amplitudes from each body but also on their relative directions. When two planets have comparable deflection scales or approach a near alignment on the sky, the geometry can lead to partial reinforcement or partial cancellation.

3.7.1 Geometry and Notation

Let the observer be E , the distant source be C , and the two planets be P_1 and P_2 . Define

$$\hat{\ell} \equiv \frac{C - E}{\|C - E\|}, \quad \hat{p}_i \equiv \frac{P_i - E}{\|P_i - E\|}, \quad r_i \equiv \|P_i - E\|, \quad i = 1, 2. \quad (3.18)$$

The planet–source separation as seen by the observer is

$$\cos \beta_i = \hat{p}_i \cdot \hat{\ell}, \quad \beta_i = \arccos(\hat{p}_i \cdot \hat{\ell}), \quad b_i = r_i \sin \beta_i. \quad (3.19)$$

The unit direction for the deflection in the tangent plane is

$$t_i = \hat{p}_i - (\hat{p}_i \cdot \hat{\ell}) \hat{\ell}, \quad \hat{n}_i = \frac{t_i}{\|t_i\|}. \quad (3.20)$$

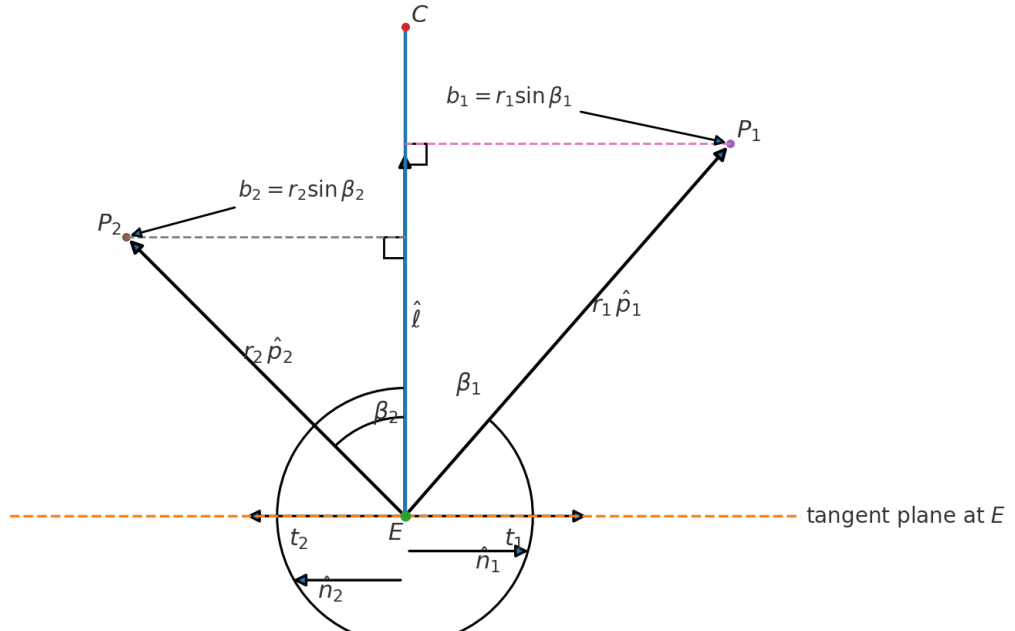


Figure 3.8: Geometry and notation for the dual-planet case: line of sight $\hat{\ell}$ from E to C ; planet directions $r_i \hat{p}_i$; angles β_i and impact parameters b_i ; projected tangent directions t_i and unit vectors \hat{n}_i .

3.7.2 Single Body Deflection and Dual Body Superposition

For a single planet P_i with mass M_i , the general form of the light deflection angle used in this work is

$$\alpha_i(\beta_i) = \frac{2GM_i}{c^2 r_i \sin \beta_i} (1 + \cos \beta_i). \quad (3.21)$$

The corresponding vector in the tangent plane is

$$\vec{\alpha}_i = \alpha_i \hat{n}_i. \quad (3.22)$$

The total deflection for two planets is the vector sum

$$\vec{\alpha}_{\text{tot}} = \vec{\alpha}_1 + \vec{\alpha}_2, \quad \alpha_{\text{tot}} = \|\vec{\alpha}_{\text{tot}}\| = \sqrt{\alpha_1^2 + \alpha_2^2 + 2\alpha_1\alpha_2 \cos \Delta\phi}, \quad (3.23)$$

where $\Delta\phi$ is the angle between \hat{n}_1 and \hat{n}_2 in the tangent plane, so that $\cos \Delta\phi = \hat{n}_1 \cdot \hat{n}_2$. For sufficiently large β_i , the far field form $\alpha_i \simeq 2GM_i/(c^2 b_i)$ follows from (3.21).

Evaluate two representative pairs:

- Jupiter and Saturn, a strong deflection case with a dominant contribution from Jupiter and a clear secondary from Saturn,
- Uranus and Neptune, a moderate deflection case with comparable contributors.

Scan the planet–source separation over

$$\beta \in \{0.1^\circ, 0.2^\circ, 0.5^\circ, 1^\circ, 2^\circ, 5^\circ, 10^\circ, 20^\circ, 45^\circ, 89^\circ\}.$$

The methodology above casts the dual–planet problem into a purely tangent–plane construction: directions are defined by the unit vectors $\hat{\ell}$ and \hat{p}_i , angular separations by β_i , impact parameters by $b_i = r_i \sin \beta_i$, and deflection directions by \hat{n}_i .

Chapter 4

Results and Analysis

4.1 Impact of Uncertainties in the Gravitational Constant G and Planetary Masses

The light deflection angle depends on the factor GM , where G is the gravitational constant and M is the mass of the deflecting body.¹ Therefore, uncertainties in either G or M will propagate into the final value of the light deflection angle. A more general and systematic way to quantify this propagation is by using the error propagation formula with the Jacobian and covariance matrix. Let

$$y = GM, \quad x = (G, M)^\top. \quad (4.1)$$

Then the variance of y can be expressed as

$$\text{Var}(y) \approx \nabla y^\top \Sigma \nabla y, \quad (4.2)$$

where

$$\nabla y = \left(\frac{\partial y}{\partial G}, \frac{\partial y}{\partial M} \right)^\top = (M, G)^\top, \quad (4.3)$$

is the Jacobian vector, and Σ is the covariance matrix of the input variables (G, M) :

$$\Sigma = \begin{bmatrix} \sigma_G^2 & \text{Cov}(G, M) \\ \text{Cov}(M, G) & \sigma_M^2 \end{bmatrix}. \quad (4.4)$$

Expanding this expression gives

$$\text{Var}(GM) = M^2 \sigma_G^2 + G^2 \sigma_M^2 + 2GM \rho \sigma_G \sigma_M, \quad (4.5)$$

where $\rho = \frac{\text{Cov}(G, M)}{\sigma_G \sigma_M}$ is the correlation coefficient. Consequently, the relative uncertainty can be written as

$$\frac{\sigma_{GM}}{GM} = \sqrt{\left(\frac{\sigma_G}{G}\right)^2 + \left(\frac{\sigma_M}{M}\right)^2 + 2\rho \frac{\sigma_G}{G} \frac{\sigma_M}{M}}. \quad (4.6)$$

Using the CODATA 2018 uncertainty in G and the measured planetary masses, the propagated uncertainties of GM for the eight planets were computed under different correlation assumptions. The results are presented in Table 4.1.¹⁹

Planet	GM (km ³ /s ²)	$\rho = 0$	$\rho = +1$	$\rho = -1$
Mercury	2.204×10^4	2.200×10^{-5}	2.201×10^{-5}	2.198×10^{-5}
Venus	3.252×10^5	2.200×10^{-5}	2.200×10^{-5}	2.200×10^{-5}
Earth	3.986×10^5	2.200×10^{-5}	2.200×10^{-5}	2.200×10^{-5}
Mars	4.281×10^4	2.200×10^{-5}	2.200×10^{-5}	2.199×10^{-5}
Jupiter	1.267×10^8	2.200×10^{-5}	2.200×10^{-5}	2.200×10^{-5}
Saturn	3.794×10^7	2.200×10^{-5}	2.200×10^{-5}	2.200×10^{-5}
Uranus	5.794×10^6	2.200×10^{-5}	2.200×10^{-5}	2.200×10^{-5}
Neptune	6.832×10^6	2.200×10^{-5}	2.200×10^{-5}	2.200×10^{-5}

Table 4.1: Relative uncertainties of GM for the eight planets under different correlation assumptions.

From Table 4.1 it is evident that, for all planets, the relative uncertainty σ_{GM}/GM is essentially fixed at the level of 2.200×10^{-5} . This indicates that the CODATA 2018 uncertainty of G completely dominates the error budget, while the uncertainties in planetary masses are smaller by 3–4 orders of magnitude and therefore negligible.

For Mercury and Mars, a minor variation can be observed in the last decimal place when $\rho = \pm 1$, with differences at the level of 10^{-8} . This arises because their mass uncertainties are slightly larger compared to other planets, allowing the correlation term to contribute beyond truncation precision. However, these deviations remain three orders of magnitude below 2.2×10^{-5} , and can be safely ignored in practical light deflection calculations.

In conclusion, the uncertainty in GM is almost entirely determined by σ_G/G . Thus, improving the accuracy of light deflection predictions requires more precise determinations of the gravitational constant G , rather than refinements in planetary mass measurements.

4.2 The Deflection Angle α

The gravitational light deflection angle is given by General Relativity as

$$\alpha = \frac{4GM}{c^2 b}, \quad (4.7)$$

where M is the mass of the deflecting body, b is the impact parameter (approximated by the body's radius).

Using a Python implementation of the above formula, computed the *maximum* gravitational deflection angles for 59 major Solar System bodies (including the Sun, planets, moons, and asteroids), expressed in microarcseconds (μas). The complete results and a comparison with the values reported by Geng (2023) and Li et al. (2022) are listed in Table 4.3. A logarithmic bar chart highlighting the wide dynamic range of these deflections is shown in Figure 4.1.

The key trends emerging from the results are as follows:

- **The Sun dominates the deflection.** Its maximum deflection reaches $1.75 \times 10^6 \mu\text{as}$, consistent with the 1919 eclipse measurement and the literature.
- **Planets span from hundreds to tens of thousands of μas .** Jupiter is largest ($1.66 \times 10^4 \mu\text{as}$), followed by Saturn ($6.0 \times 10^3 \mu\text{as}$). Earth and Venus yield $574 \mu\text{as}$ and $493 \mu\text{as}$, respectively, while Pluto is the smallest among planets at $6.7 \mu\text{as}$.
- **The Moon and large satellites are non-negligible.** The Moon is $26 \mu\text{as}$; among Jupiter's Galilean moons, Ganymede is $35 \mu\text{as}$ and the others exceed $18 \mu\text{as}$; Titan reaches $32 \mu\text{as}$. These can matter for μas -level astrometry.
- **Medium/small satellites and most asteroids are much smaller.** Nine moons exceed $1 \mu\text{as}$ (e.g., Titania, Oberon, Ariel, Umbriel, Triton, Charon). Among asteroids, only Ceres exceeds $1 \mu\text{as}$ ($1.22 \mu\text{as}$); Pallas, Vesta, and Hygiea lie between 0.3 – $0.6 \mu\text{as}$.

In conclusion, the Sun and planets dominate the signal, yet at μas accuracy the contributions from large moons and several asteroids must also be modeled, especially for ultra-precise radio interferometry such as the SKA. Finally, while planetary mass and radius are known with high precision, the overall theoretical uncertainty of α is chiefly limited by the precision of G ; the current CODATA relative uncertainty is 2.2×10^{-5} , which sets the fundamental limit in this work.

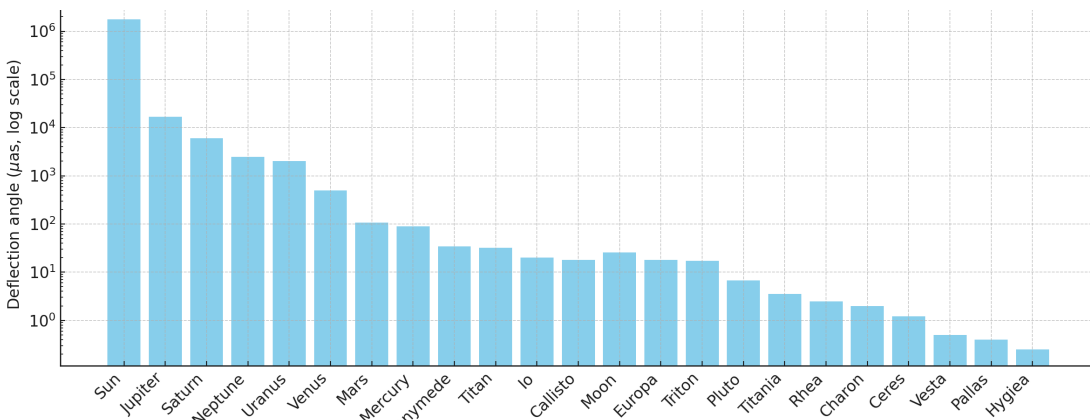


Figure 4.1: Maximum gravitational deflection (logarithmic scale) for Solar System bodies.

The results of the following table show excellent agreement with previous works, and are particularly consistent with the authoritative values reported by Li et al.²³

Body	Mass (kg)	Radius (km)	α_{\max} (μas)	α_{\max} by Geng	α_{\max} by Li
Sun	1.9885×10^{30}	695700	1.7513×10^6	1.7511×10^6	1.7512×10^6
Mercury	3.3010×10^{23}	2439.7	82.90	82.90	82.91
Venus	4.8673×10^{24}	6051.8	492.78	492.75	492.78
Moon	7.3460×10^{22}	1738.1	25.90	25.89	25.90
Mars	6.4169×10^{23}	3389.5	115.99	115.99	116.00
Phobos	1.0659×10^{14}	11.1	0.00	0.00	0.00
Deimos	1.4762×10^{15}	6.2	0.00	0.00	0.00
Jupiter	1.8981×10^{27}	69911	1.6635×10^4	1.6634×10^4	1.6635×10^4
Io	8.9319×10^{22}	1821.6	30.04	30.04	30.04
Europa	4.7998×10^{22}	1560.8	18.84	18.84	18.84
Ganymede	1.4819×10^{23}	2631.2	34.51	34.51	34.50
Callisto	1.0759×10^{23}	2410.3	27.35	27.35	27.34
Saturn	5.6832×10^{26}	58232	5979.72	5979.31	5979.49
Titan	1.3455×10^{23}	2574.7	32.02	32.02	32.01
Rhea	2.3100×10^{21}	764.3	1.85	1.85	1.85
Iapetus	1.8100×10^{21}	735.6	1.51	1.51	1.50
Dione	1.1000×10^{21}	561.7	1.20	1.20	1.19
Tethys	6.1800×10^{20}	533.0	0.71	0.71	0.71
Enceladus	1.0800×10^{20}	252.1	0.26	0.26	0.26
Mimas	3.7900×10^{19}	198.2	0.12	0.12	0.12
Phoebe	8.3000×10^{18}	106.5	0.05	0.05	0.05
Hyperion	5.6000×10^{18}	135.0	0.03	0.03	0.03
Janus	1.9000×10^{18}	89.5	0.01	0.01	0.01
Epimetheus	5.3000×10^{17}	58.1	0.01	0.01	0.01
Prometheus	1.6000×10^{17}	43.1	0.00	0.00	0.00
Pandora	1.4000×10^{17}	40.7	0.00	0.00	0.00
Uranus	8.6811×10^{25}	25362	2097.20	2097.06	2097.18
Titania	3.4200×10^{21}	788.9	2.66	2.66	2.66
Oberon	2.8834×10^{21}	761.4	2.32	2.32	2.32
Ariel	1.2948×10^{21}	578.9	1.37	1.37	1.37
Umbriel	1.2214×10^{21}	584.7	1.28	1.28	1.28
Miranda	6.5941×10^{19}	235.8	0.17	0.17	0.17
Neptune	1.0241×10^{26}	24622	2548.38	2548.20	2548.39

Body	Mass (kg)	Radius (km)	α_{\max} (μ as)	α_{\max} by Geng	α_{\max} by Li
Triton	2.1395×10^{22}	1353.4	9.69	9.69	9.68
Proteus	5.0355×10^{19}	210.0	0.15	0.15	0.15
Nereid	3.0873×10^{19}	170.0	0.11	0.11	0.11
Larissa	4.9456×10^{18}	97.0	0.03	0.03	0.03
Galatea	3.7467×10^{18}	88.0	0.03	0.03	0.03
Despina	2.0981×10^{18}	75.0	0.02	0.02	0.02
Thalassa	3.7467×10^{17}	41.0	0.01	0.01	0.01
Naiad	1.9483×10^{17}	33.0	0.00	0.00	0.00
Halimede	8.9920×10^{16}	31.0	0.00	0.00	0.00
Neso	1.6485×10^{17}	30.0	0.00	0.00	0.00
Sao	8.9920×10^{16}	22.0	0.00	0.00	0.00
Laomedea	8.9920×10^{16}	21.0	0.00	0.00	0.00
Psamathe	1.4987×10^{16}	20.0	0.00	0.00	0.00
Hippocamp	1.4987×10^{16}	9.0	0.00	0.00	0.00
Pluto	1.3030×10^{22}	1188	6.72	6.72	6.72
Charon	1.5466×10^{21}	603.6	1.57	1.57	1.56
Hydra	9.8912×10^{17}	36.0	0.02	0.02	0.00
Ceres	9.4700×10^{20}	476.2	1.22	1.22	1.22
Pallas	2.1400×10^{20}	272.5	0.48	0.48	0.48
Vesta	2.5900×10^{20}	262.7	0.60	0.60	0.60
Hygiea	1.0500×10^{20}	203.6	0.32	0.32	0.32
Interamnia	7.4900×10^{19}	153.2	0.30	0.30	0.30
Psyche	2.2900×10^{19}	113.0	0.12	0.12	0.12
Kalliope	7.3600×10^{18}	83.8	0.05	0.05	0.05
Camilla	1.1200×10^{18}	105.2	0.01	0.07	0.07

Table 4.3: Comparison of gravitational light deflection angles (μ as) for 59 Solar System bodies. Columns show the adopted mass and radius, the results of this study, and reference values from Geng (2023) and Li et al. (2022).

4.3 Impact Ranges

In this study I compute the angular impact range β for major Solar System bodies at three deflection thresholds, 10 μ as, 1 μ as, and 0.1 μ as, and compare the results at the geocentric minimum and maximum distances within one synodic cycle.

The Sun nearly covers the whole range. At 10 μ as the impact angle is about 179.7°; even at 0.1 μ as it remains 179.997°, which is practically full sky coverage. Among planets, Jupiter is the strongest contributor: at 10 μ as its impact range spans 7.18° to 10.58°; at 1 μ as it expands to 64.2° to 85.6°; at 0.1 μ as it reaches 161.9° to 167.7°. Saturn follows: 1.26° to 1.55° at 10 μ as, 12.6° to 15.4° at 1 μ as, and 95.5° to 107.2° at 0.1 μ as. Venus shows strong threshold sensitivity: 0.07° to 0.41° (10 μ as), 0.66° to 4.08° (1 μ as), and 6.63° to 39.2° (0.1 μ as). The Moon, though low mass, produces a strong local effect because of proximity: 0.67° (10 μ as), 6.70° (1 μ as), and 60.7° (0.1 μ as). For distant outer planets, Uranus and Neptune remain at about 0.10° and 0.08° at 10 μ as and reach about 10° and 8° at 0.1 μ as. Small bodies and satellites stay in the 10⁻³ to 10⁻² degree band and are usually negligible except for extreme near-grazing geometries.

Body	β_{\max}^{10}	β_{\min}^{10}	β_{\max}^1	β_{\min}^1	$\beta_{\max}^{0.1}$	$\beta_{\min}^{0.1}$
Sun	179.7186	179.7186	179.9719	179.9719	179.9972	179.9972
Mercury	0.0127	0.0056	0.1270	0.0557	1.2698	0.5573
Venus	0.4079	0.0664	4.0776	0.6641	39.1903	6.6333
Moon	0.6705	0.6705	6.6974	6.6974	60.6661	60.6661
Mars	0.0290	0.0060	0.2896	0.0598	2.8952	0.5976
Jupiter	10.5754	7.1750	85.5691	64.1719	167.6664	161.8753
Saturn	1.5543	1.2605	15.4497	12.5551	107.2040	95.4549
Uranus	0.1119	0.1008	1.1192	1.0084	11.1574	10.0587
Neptune	0.0827	0.0774	0.8273	0.7740	8.2584	7.7281
Pluto	0.0000	0.0000	0.0001	0.0001	0.0008	0.0008
Ceres	0.0000	0.0000	0.0001	0.0001	0.0012	0.0006
Pallas	0.0000	0.0000	0.0000	0.0000	0.0003	0.0001
Vesta	0.0000	0.0000	0.0000	0.0000	0.0004	0.0002
Ganymede	0.0008	0.0006	0.0083	0.0056	0.0828	0.0561
Callisto	0.0006	0.0004	0.0060	0.0041	0.0601	0.0407
Io	0.0005	0.0003	0.0050	0.0034	0.0499	0.0338
Europa	0.0003	0.0002	0.0027	0.0018	0.0268	0.0182
Titan	0.0004	0.0003	0.0037	0.0030	0.0368	0.0298
Eris	0.0000	0.0000	0.0001	0.0001	0.0006	0.0006

Table 4.4: Impact angle β in degrees at three thresholds. Superscripts 10, 1, and 0.1 denote 10 μ as, 1 μ as, and 0.1 μ as, respectively.

Distance max versus min

Within a circular-orbit approximation take

$$r_{\min} = |R - 1| \text{ AU}, \quad r_{\max} = (R + 1) \text{ AU}, \quad (4.8)$$

where R is the planetary semi-major axis in AU. Using the analytic inversion adopted in this work,

$$\beta(r, \alpha) = 2 \arctan\left(\frac{2GM}{c^2 r \alpha}\right), \quad (4.9)$$

β decreases monotonically with r , so β_{\max} comes from r_{\min} and β_{\min} from r_{\max} .

For small angles one obtains a simple geometric ratio

$$\frac{\beta(r_{\min})}{\beta(r_{\max})} \approx \Lambda = \begin{cases} \frac{1+R}{1-R}, & R < 1, \\ \frac{1+R}{R-1}, & R > 1, \end{cases} \quad (4.10)$$

which our numbers verify: for Venus ($R = 0.72$) the $1 \mu\text{as}$ ratio $4.0776^\circ/0.6641^\circ = 6.14$ equals $\Lambda = 6.14$; for Mercury ($R = 0.39$) all thresholds give ratios about 2.28, matching $\Lambda = 2.28$; for Mars ($R = 1.52$) the ratios are 4.83 to 4.85, consistent with $\Lambda = 4.85$. For Jupiter and Saturn the ratio agrees with Λ at $10 \mu\text{as}$ but drops toward 1.33 and 1.04 for Jupiter at $1 \mu\text{as}$ and $0.1 \mu\text{as}$, and to 1.12 for Saturn at $0.1 \mu\text{as}$, indicating saturation at large β where distance sensitivity weakens.

A practical single number to quantify scheduling gain is the difference

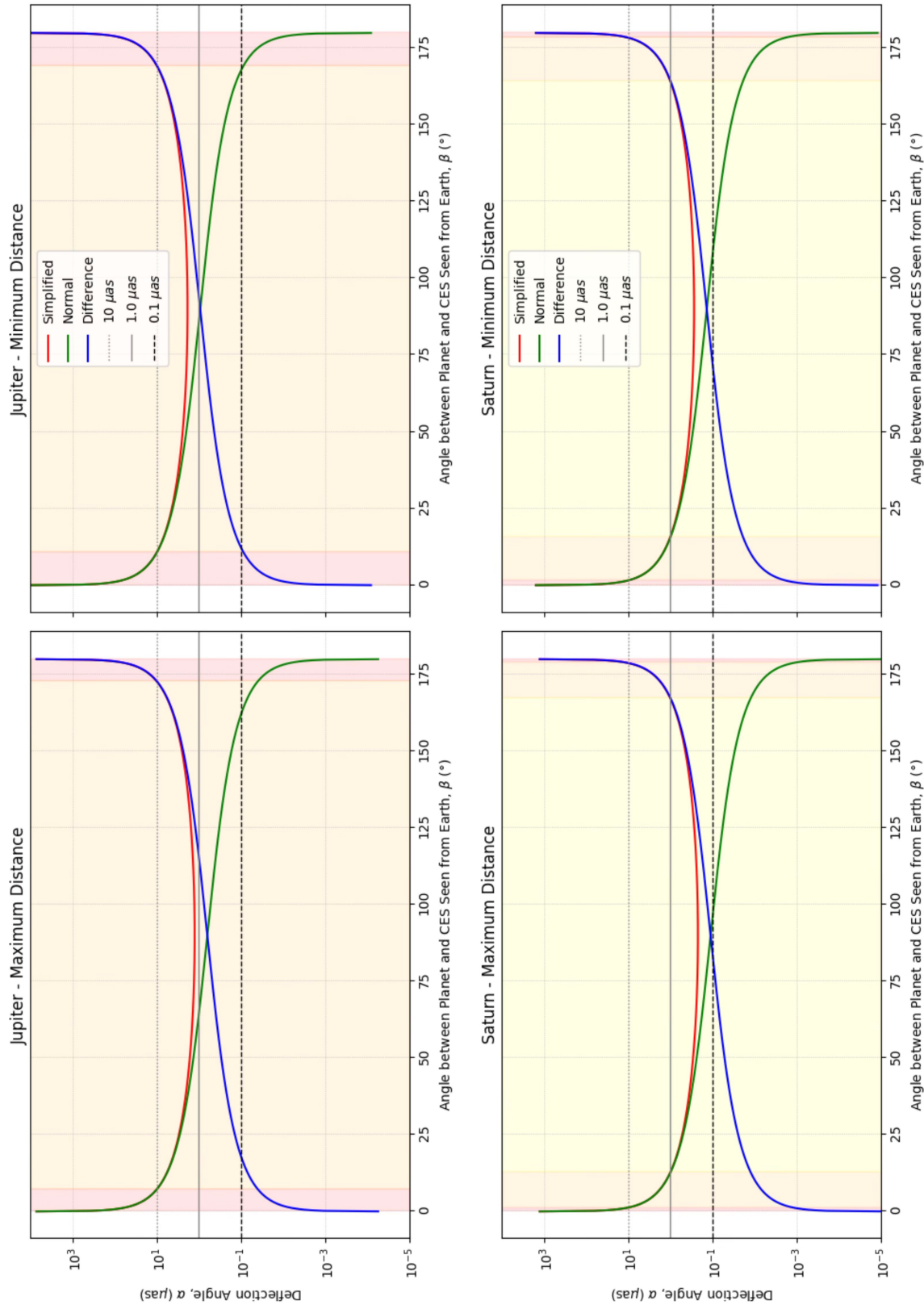
$$\Delta\beta(\alpha) = \beta(r_{\min}, \alpha) - \beta(r_{\max}, \alpha). \quad (4.11)$$

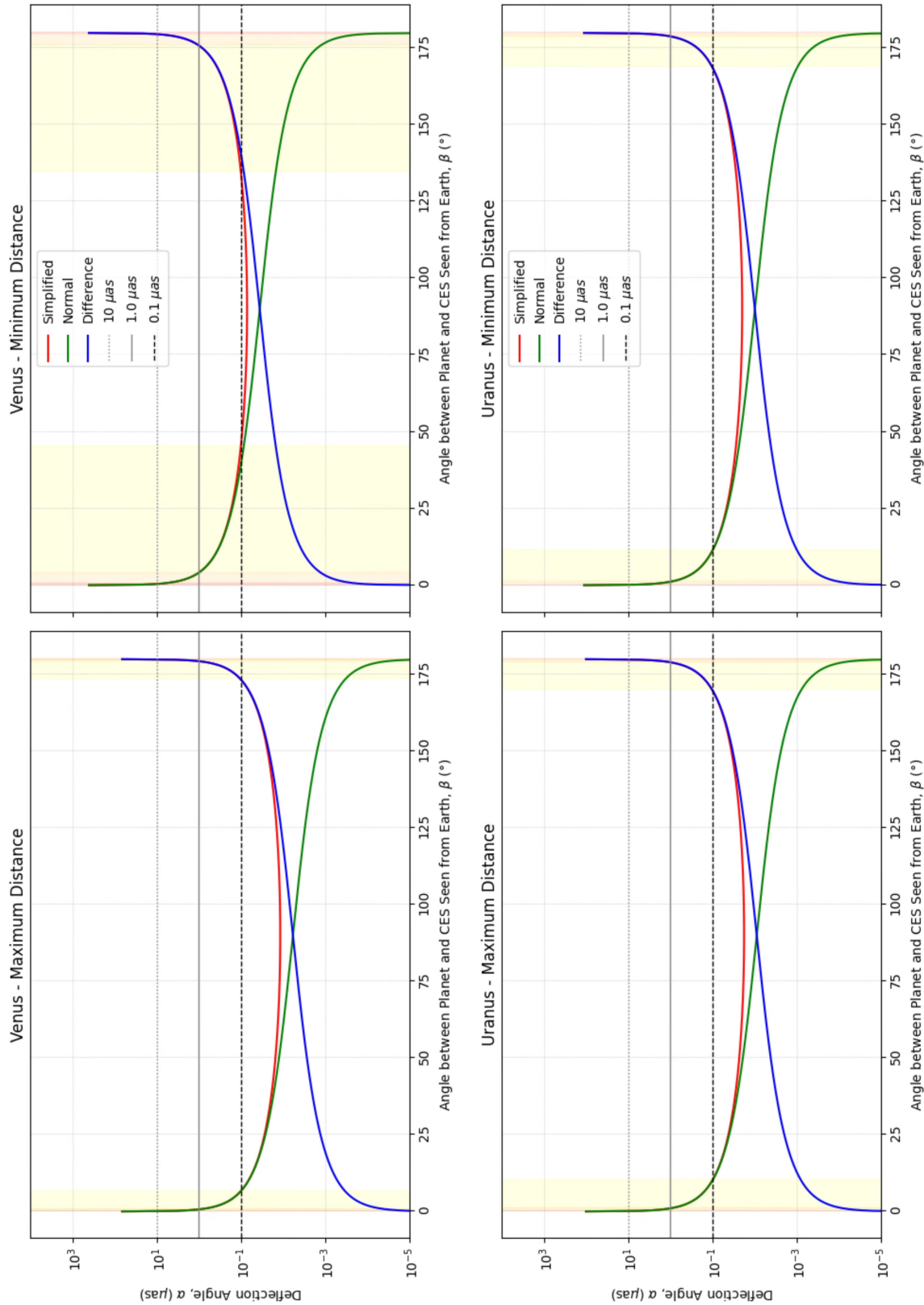
Representative values are: Jupiter 3.40° ($10 \mu\text{as}$), 21.40° ($1 \mu\text{as}$), 5.79° ($0.1 \mu\text{as}$); Venus 0.34° , 3.41° , 32.56° ; Saturn 0.29° , 2.89° , 11.75° ; Neptune 0.053° at $1 \mu\text{as}$. These numbers motivate observing near r_{\max} for inner planets and explicit modeling for giant planets at sub-microarcsecond goals.

To visually compare the deflection strength under the two geometries r_{\max} and r_{\min} , plot for each planet a pair of panels (left: r_{\max} , right: r_{\min}) as follows. For each fixed distance r and an angle grid $\beta \in [0.01^\circ, 179.99^\circ]$, compute

$$\alpha_{\text{normal}} = \frac{2GM}{c^2 r \sin \beta} (1 + \cos \beta), \quad \alpha_{\text{simplified}} = \frac{4GM}{c^2 r \sin \beta}, \quad \alpha_{\text{diff}} = \alpha_{\text{simplified}} - \alpha_{\text{normal}}. \quad (4.12)$$

Using the red curve as the reference, shade the background according to the deflection level: $\alpha_{\text{simplified}} > 10 \mu\text{as}$ (light red), $1 \mu\text{as} < \alpha_{\text{simplified}} \leq 10 \mu\text{as}$ (orange), $0.1 \mu\text{as} < \alpha_{\text{simplified}} \leq 1 \mu\text{as}$ (yellow), and no shading for $\alpha_{\text{simplified}} \leq 0.1 \mu\text{as}$.

Figure 4.2: Threshold maps (I): Saturn and Jupiter. Left: r_{\max} ; Right: r_{\min} .

Figure 4.3: Threshold maps (II): Venus and Uranus. Left: r_{\max} ; Right: r_{\min} .

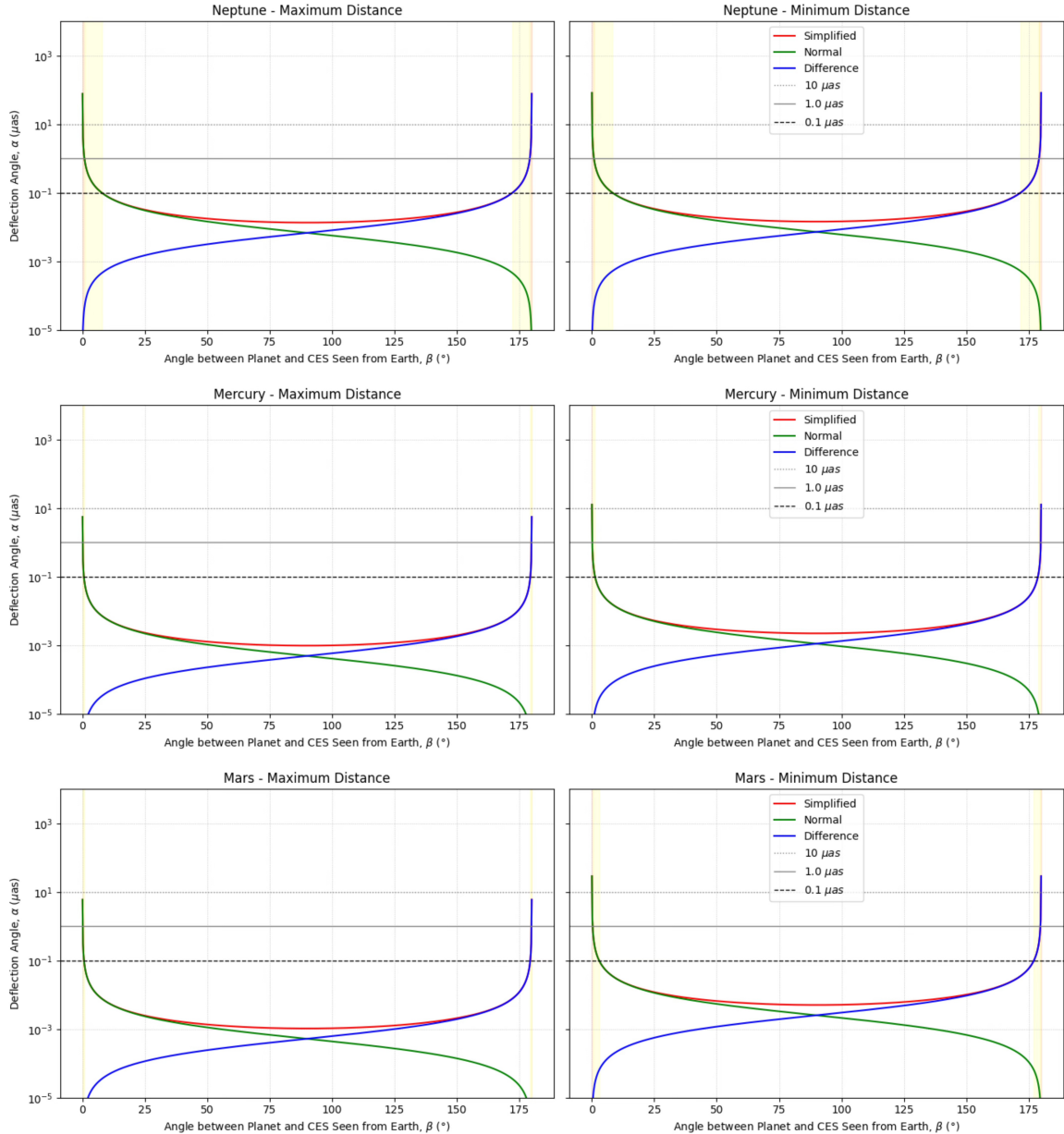


Figure 4.4: Threshold maps (III): Neptune, Mercury, and Mars. Left: r_{\max} ; Right: r_{\min} .

Figures above show a clear distance amplification: for the same planet, the high-deflection shaded bands are wider at r_{\min} than at r_{\max} , and the intersections with the threshold lines shift to larger angular coverage. The contrast is strongest for Venus and Mercury (consistent with the geometric leverage), while Uranus and Neptune display almost overlapping panels, indicating weak distance sensitivity.

For the giant planets (Jupiter, Saturn), the gap between the two panels narrows at strict thresholds, evidencing large- β saturation and reduced sensitivity to distance. The simplified and geometry-corrected models agree in the mid- β and differ only near the ends, which fall largely within the inaccessible bands.

4.4 Differentiation Based Analysis of $\alpha(\beta)$ and the Impact Ranges

4.4.1 Geometry to Deflection

Starting from the geometric relation and working expression

$$b = r \sin \beta \text{ (Eq. 3.19), } \alpha(\beta) = \frac{2GM}{c^2 r \sin \beta} (1 + \cos \beta) = \frac{2GM}{c^2 r} \cot \frac{\beta}{2}, \quad (4.13)$$

the partial derivatives with respect to (GM, r, β) are

$$\frac{\partial \alpha}{\partial (GM)} = \frac{\alpha}{GM}, \quad \frac{\partial \alpha}{\partial r} = -\frac{\alpha}{r}, \quad \frac{\partial \alpha}{\partial \beta} = -\frac{\alpha}{\sin \beta}. \quad (4.14)$$

Hence the first-order total differential separates mass, distance and geometry:

$$\frac{d\alpha}{\alpha} = \frac{d(GM)}{GM} - \frac{dr}{r} - \frac{d\beta}{\sin \beta}$$

(4.15)

so the geometric term dominates when β is small because $\sin \beta \approx \beta$. This explains the strong geometric leverage in Table 4.4 for inner planets. For Venus at the $1 \mu\text{as}$ threshold the two endpoints of the impact range are 0.6641° and 4.0776° ; their ratio equals the analytic small-angle factor $\Lambda = (1 + R)/(1 - R) = 6.14$, confirming that the geometric contribution $-d\beta/\sin \beta$ controls the variation at this threshold.

Second derivatives quantify curvature:

$$\frac{\partial^2 \alpha}{\partial \beta^2} = \frac{\alpha}{2 \sin^2(\beta/2)}, \quad \frac{\partial^2 \alpha}{\partial r^2} = \frac{2\alpha}{r^2}, \quad \frac{\partial^2 \alpha}{\partial r \partial \beta} = \frac{\alpha}{r \sin \beta}. \quad (4.16)$$

As $\beta \rightarrow 0$, $\sin(\beta/2)$ becomes very small and the angular curvature grows rapidly, which is the high sensitivity of near-grazing bands seen in the threshold maps.

4.4.2 Implicit Differentiation of β

From the analytic inversion (Eq. 4.9) under the circular-orbit approximation (Eq. 4.8),

$$\beta(r, \alpha) = 2 \arctan\left(\frac{2GM}{c^2 r \alpha}\right), \quad (4.17)$$

implicit differentiation gives two compact sensitivities

$$\left. \frac{\partial \beta}{\partial r} \right|_\alpha = -\frac{\sin \beta}{r} < 0, \quad \left. \frac{\partial \beta}{\partial \alpha} \right|_r = -\frac{4GM}{c^2 r} \frac{1}{\alpha^2 + (\frac{2GM}{c^2 r})^2} < 0.$$

(4.18)

The first proves that β decreases with distance, hence β_{\max} always occurs at r_{\min} and β_{\min} at r_{\max} (as in Table 4.4). The second shows that a tighter threshold (smaller α) expands the angular domain, but the expansion saturates once the denominator is dominated by the geometric constant term.

These derivatives align point-by-point with the tabulated values. For Jupiter, tightening the threshold from 10 μas to 1 μas expands β from $7.18^\circ \sim 10.58^\circ$ to $64.17^\circ \sim 85.57^\circ$ (strong negative sensitivity $\partial\beta/\partial\alpha < 0$). Further tightening to 0.1 μas pushes β close to 180° ($161.88^\circ \sim 167.67^\circ$); the response has entered the saturated regime, and the two-end difference $\Delta\beta = \beta(r_{\min}) - \beta(r_{\max})$ shrinks from 21.40° to 5.79° , consistent with $\partial\beta/\partial r = -\sin\beta/r$ becoming small when β is large.

For Venus, at 1 μas the ratio $4.0776^\circ/0.6641^\circ = 6.14$ matches Λ , showing the near-grazing regime is still in control; when tightening to 0.1 μas the range jumps to $6.63^\circ \sim 39.19^\circ$ and $\Delta\beta$ to 32.56° , which is the strong-response phase predicted by $\partial\beta/\partial\alpha < 0$. Representative $\Delta\beta$ values in Table 4.4 are Jupiter $3.40^\circ, 21.40^\circ, 5.79^\circ$, Venus $0.34^\circ, 3.41^\circ, 32.56^\circ$, Saturn $0.29^\circ, 2.89^\circ, 11.75^\circ$ for thresholds 10, 1, 0.1 μas .

4.4.3 Endpoint Expansions

Writing $\alpha = \frac{2GM}{c^2r} \cot(\beta/2)$, the two endpoint expansions give the orders of divergence or saturation.

Near-grazing limit $\beta \rightarrow 0$. Using $\cot(\beta/2) = 2/\beta - \beta/6 - \beta^3/360 + \dots$,

$$\alpha \simeq \frac{4GM}{c^2r} \frac{1}{\beta} \left[1 - \frac{\beta^2}{12} + O(\beta^4) \right], \quad \frac{\partial\alpha}{\partial\beta} \simeq -\frac{4GM}{c^2r} \frac{1}{\beta^2}. \quad (4.19)$$

The first derivative diverges as β^{-2} , explaining why small angular changes produce large changes of α for Mercury and Venus, and why their impact ranges expand quickly when the threshold is tightened.

Reverse limit $\beta = \pi - \varepsilon \rightarrow \pi$. Since $\cot(\beta/2) = \tan(\varepsilon/2)$,

$$\alpha \simeq \frac{GM}{c^2r} \varepsilon \left[1 + \frac{\varepsilon^2}{12} + O(\varepsilon^4) \right], \quad \frac{\partial\alpha}{\partial\beta} \xrightarrow[\varepsilon \rightarrow 0]{} -\frac{GM}{c^2r}. \quad (4.20)$$

The derivative tends to a finite constant and geometry becomes saturated. Consistently, from Eq. (4.9) one has $\frac{\partial\beta}{\partial r} = -\frac{\sin\beta}{r} \simeq -\frac{\varepsilon}{r}$, so distance changes move the boundary slowly when β approaches 180° . This is precisely what the Jupiter and Saturn panels show at the strictest threshold, matching the small $\Delta\beta$ for Jupiter at 0.1 μas (5.79°) in Table 4.4.

4.5 Perturbation Duration of Light Deflection

To quantify the impact of Solar System bodies on astrometric light deflection at different measurement precisions, evaluate the *perturbation duration* for three thresholds, namely $10\ \mu\text{as}$, $1\ \mu\text{as}$, and $0.1\ \mu\text{as}$. For a given threshold α_{th} , the duration is mapped from the angular span $\Delta\beta$ (the range of elongation angles β for which $\alpha(\beta) \geq \alpha_{\text{th}}$) to time through the synodic period T_{syn} :

$$\tau(\alpha_{\text{th}}) = \frac{\Delta\beta}{180^\circ} T_{\text{syn}}. \quad (4.21)$$

Table 4.5 summarizes the resulting durations for the main Solar System bodies at the three thresholds. Here, τ_{10} , $\tau_{1.0}$, and $\tau_{0.1}$ denote the durations for $10\ \mu\text{as}$, $1\ \mu\text{as}$, and $0.1\ \mu\text{as}$, respectively. An ellipsis indicates near full coverage over the considered synodic interval.

Object	τ_{10} (days)	$\tau_{1.0}$ (days)	$\tau_{0.1}$ (days)
Mercury	0.000	0.075	0.753
Venus	1.285	11.882	113.682
Mars	0.039	0.897	9.164
Jupiter	23.453	166.423	181.699
Saturn	3.251	29.300	193.041
Uranus	0.203	2.033	20.275
Neptune	0.147	1.525	15.250
Pluto	0.000	0.000	0.000
Moon	0.104	0.949	8.440

Table 4.5: Perturbation duration of major Solar–System bodies at different deflection thresholds (days).

The data reveal that Jupiter and Saturn dominate the perturbation budget. For Jupiter, the duration above $1\ \mu\text{as}$ reaches about 166 days, and at $0.1\ \mu\text{as}$ it approaches half a synodic period, underscoring a strong, long lasting influence on precision astrometry. Saturn, while less massive, still yields about 29 days above $1\ \mu\text{as}$ and about 193 days above $0.1\ \mu\text{as}$, which likewise requires explicit correction in high precision analyses.

Venus exceeds 110 days at the $0.1\ \mu\text{as}$ level, highlighting its relevance for sub microarcsecond programs. By contrast, Mars is weaker overall, yet still contributes about 9 days above $0.1\ \mu\text{as}$, which can matter during specific observing windows. Uranus and Neptune show shorter durations (about 20.3 and 15.3 days at $0.1\ \mu\text{as}$, respectively); although smaller than those of Jupiter and Saturn, they may accumulate into a systematic floor for ultra precise, long term campaigns. The Moon, despite its small mass, produces about 8.4 days above

$0.1 \mu\text{as}$ due to its proximity, and therefore warrants routine mitigation in very high precision experiments.

Taken together, these results indicate that Jupiter and Saturn provide the most significant and long lasting deflection at high thresholds; Venus and the Moon can be non negligible at specific precision goals; and the remaining bodies are generally of limited impact for most high precision astrometric measurements.

Jupiter: Consistency Check

Figure 4.5 shows Jupiter's deflection curves in Cartesian coordinates (semi-logarithmic y-axis) at the two geometric extremes, $r = r_{\min}$ and $r = r_{\max}$. The horizontal dashed line marks the $10 \mu\text{as}$ threshold. Four vertical dotted lines indicate the model critical elongations obtained from $\alpha(\beta) = 10 \mu\text{as}$, namely $\beta_{\text{crit}}(r_{\max})$ to $\beta_{\text{crit}}(r_{\min})$ and their symmetric positions near 180° . Duration at $10 \mu\text{as}$, $\tau_{10} = 23.453$ days, implies a single-limb half-span $\Delta\beta/2 \approx 5.29^\circ$, shown as pale vertical bands near 0° and 180° . This half-span is strictly smaller than and comparable to the model upper bound, $\beta_{\text{crit}}(r_{\max}) \approx 7.18^\circ$ to $\beta_{\text{crit}}(r_{\min}) \approx 10.57^\circ$. The close agreement between the duration-implied angular window and the physics-based critical angles confirms that Jupiter's τ_{10} is consistent with the underlying deflection model.

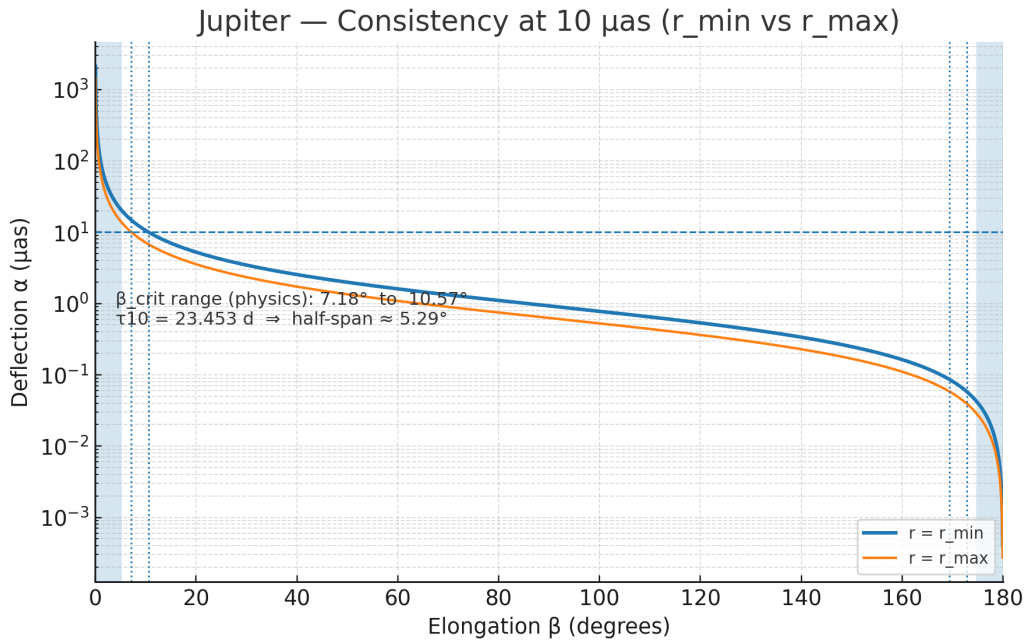


Figure 4.5: Jupiter consistency check (Cartesian, semi-log y). Pale vertical bands: half-span implied by this work, $\Delta\beta/2 \approx 5.29^\circ$ from $\tau_{10} = 23.453$ days, which lies within the model bracket, demonstrating consistency.

4.6 Dual-Planet Linear Superposition Results

In Section 3.7, I established a linear superposition model for dual-planet light deflection. The idea is that when a light ray passes through the gravitational fields of two planets, the two single-body deflection vectors can be added on the sky tangent plane to obtain the total deflection. This approximation is adequate at the microarcsecond level, and is especially suitable for planet pairs that are well separated on the sky.³

The deflection direction of each body is determined by the tangent plane vector n^i , and the total deflection for two bodies is given by:

$$\vec{\alpha}_{\text{tot}} = \vec{\alpha}_1 + \vec{\alpha}_2, \quad \alpha_{\text{tot}} = |\vec{\alpha}_{\text{tot}}|.$$

In the table below, I set the directions of the two planets within the tangent plane to differ by $\Delta\phi = 30^\circ$ for illustration.

β_{deg}	α_{Jupiter}	α_{Saturn}	α_{total}	β_{deg}	α_{Uranus}	α_{Neptune}	α_{total}
0.1	856.582430	140.383195	980.673048	0.1	10.609993	7.984269	17.973530
0.2	428.290889	70.191544	490.336151	0.2	5.304992	3.992131	8.986758
0.5	171.315442	28.076468	196.133415	0.5	2.121986	1.596844	3.594684
1.0	85.656090	14.037967	98.064840	1.0	1.060973	0.798407	1.797308
2.0	42.824783	7.018449	49.028686	2.0	0.530446	0.399173	0.898585
5.0	17.120779	2.805883	19.601017	5.0	0.212065	0.159584	0.359243
10.0	8.544071	1.400267	9.781826	10.0	0.105830	0.079640	0.179279
20.0	4.239336	0.694774	4.853477	20.0	0.052510	0.039515	0.088953
45.0	1.804647	0.295759	2.066081	45.0	0.022353	0.016821	0.037867
89.0	0.760671	0.124665	0.870867	89.0	0.009422	0.007090	0.015961

Table 4.7: Jupiter-Saturn and Uranus-Neptune linear superposition table (units: μas).

For **Jupiter–Saturn**, at a very small angular separation ($\beta = 0.1^\circ$) the total deflection approaches ~ 1 mas and is dominated by Jupiter; as the separation increases, the deflection decreases rapidly. Saturn’s contribution is about one sixth of Jupiter’s, yet its presence is still clearly visible in the total via vector superposition.

For **Uranus–Neptune**, the total deflection is about two orders of magnitude smaller than for the J–S pair. However, because the two single-body contributions are comparable, the dual-body superposition is relatively more evident; for example, at $\beta = 0.1^\circ$ the total is $\approx 18 \mu\text{as}$, nearly equal to the sum of the two.

At all separations the dual-body total closely follows the near sum of the individual deflections, with no anomalous interference or nonlinear signatures, thereby validating the linear-superposition assumption adopted in Section 3.7.

Figure 4.6 compare the single-body deflections (Jupiter, Saturn) with their total. The total curve almost coincides with Jupiter’s curve, indicating that Jupiter dominates this pair; at the same time, Saturn consistently lifts the total across all angular separations. For $\beta = 0.1^\circ$ we have $\alpha_J \approx 856.6 \mu\text{as}$, $\alpha_S \approx 140.4 \mu\text{as}$, and $\alpha_{\text{tot}} \approx 980.7 \mu\text{as}$, an $\sim 14\%$ increase relative to modeling Jupiter alone. The same fractional uplift is seen at $\beta = 1^\circ$ and 10° . This behavior is fully consistent with Section 3.7: the total deflection lies between the largest single-body curve and the algebraic sum of the two, and the relative spacing remains nearly constant over the full β range.

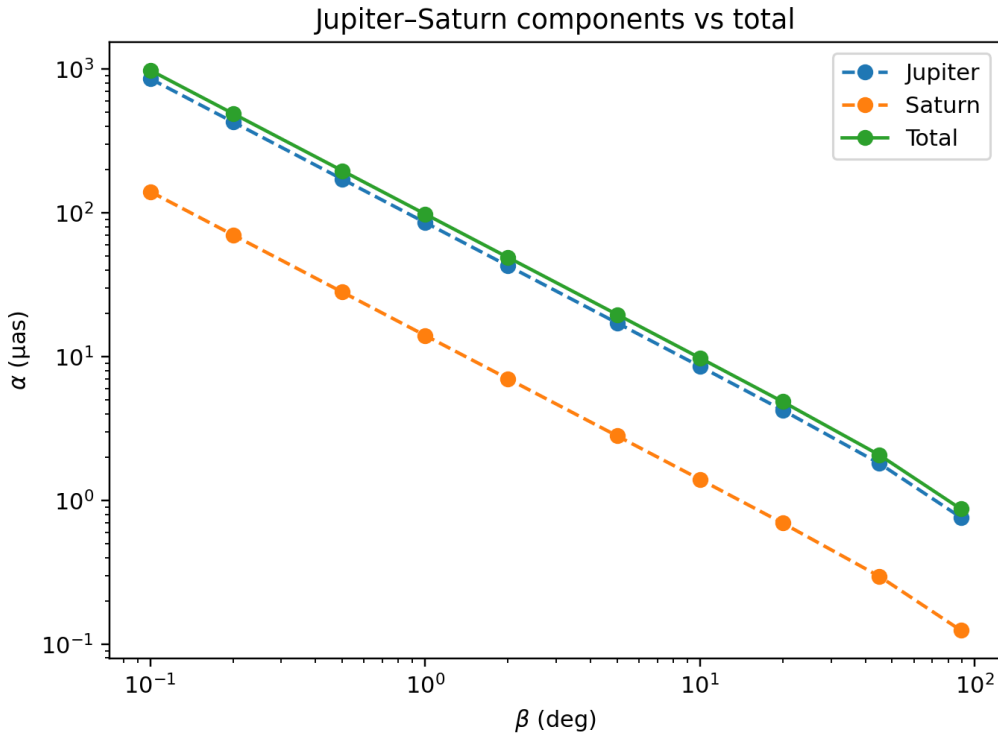


Figure 4.6: Jupiter–Saturn components vs total. The total deflection almost coincides with Jupiter’s curve, with a nearly constant fractional uplift due to Saturn across β .

Figure 4.7 shows that the single-body curves for Uranus and Neptune lie close to each other, indicating comparable contributions. Consequently, the total deflection is very close to their algebraic sum. At $\beta = 0.1^\circ$, the total is $\alpha_{\text{tot}} \approx 18 \mu\text{as}$, nearly equal to $\alpha_U + \alpha_N$. As β increases, the three curves remain nearly parallel, indicating that the geometry mainly manifests through vector addition rather than altering the β -scaling. This is fully consistent with Section 3.7, where the two deflection vectors are added on the sky tangent plane.

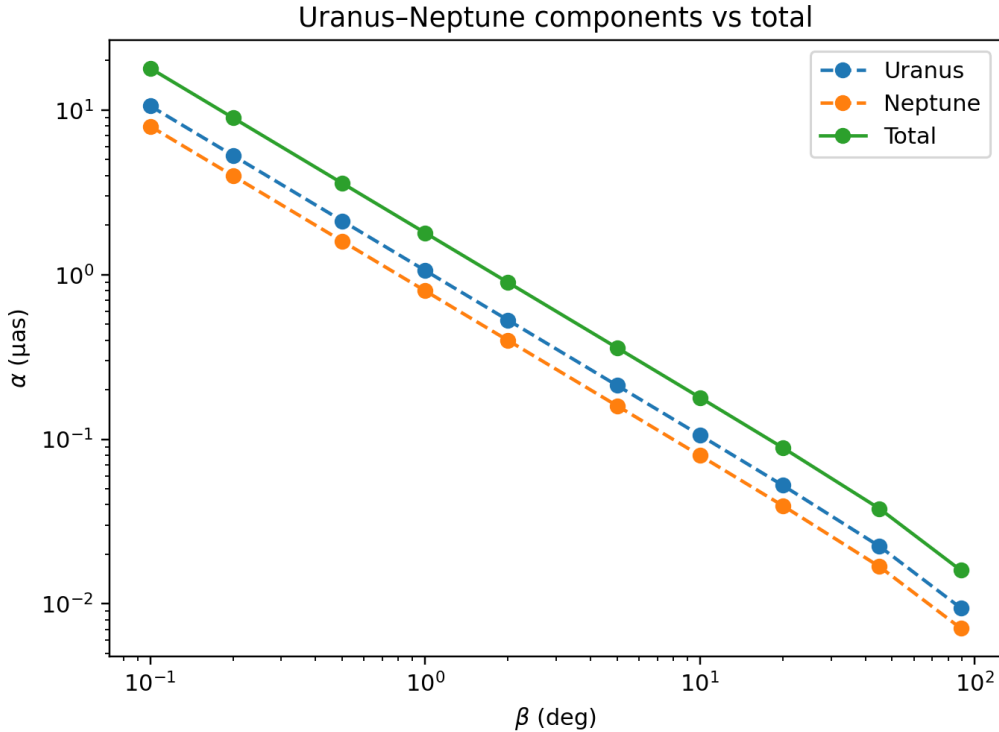


Figure 4.7: Uranus–Neptune components vs total. The total closely follows the algebraic sum because the two single-body contributions are comparable across β .

Under the linear superposition in Section 3.7, the dual-planet deflection obeys

$$\alpha_{\text{tot}} = \sqrt{\alpha_1^2 + \alpha_2^2 + 2\alpha_1\alpha_2 \cos \Delta\phi}, \quad \alpha_i(\beta) \propto \frac{1 + \cos \beta}{\sin \beta} = \cot \frac{\beta}{2},$$

so at small β we have $\alpha \propto 1/\beta$. Numerically, for Jupiter–Saturn $\alpha_{\text{tot}}(0.1^\circ) \approx 980.7 \mu\text{as}$ and $\alpha_{\text{tot}}(1^\circ) \approx 98.06 \mu\text{as}$; for Uranus–Neptune $\alpha_{\text{tot}}(0.1^\circ) \approx 17.97 \mu\text{as}$. Within each pair the single-body ratio is nearly constant with β ($\alpha_J/\alpha_S \approx 6.1$, $\alpha_U/\alpha_N \approx 1.33$), reflecting fixed M/r contrasts. With the illustrative $\Delta\phi = 30^\circ$, the vector nature yields a mild reduction relative to the algebraic sum, $f = \alpha_{\text{tot}}/(\alpha_1 + \alpha_2) \approx 0.984$ (J–S) and ≈ 0.967 (U–N). These results validate the linear superposition and motivate including at least dual-body terms in microarcsecond astrometric modeling, with $\Delta\phi$ evaluated from the actual geometry.

Chapter 5

Conclusion and Future Work

5.1 Conclusion

In this study, based on the theory of gravitational light deflection and using the JPL DE440s ephemerides, systematically computed the deflection effects of 59 major Solar System bodies. A Python-based numerical implementation was employed, and the results were compared with previous works for validation.

First, regarding the maximum deflection angles, our calculations are in excellent agreement with the authoritative results reported by Li et al. (2022) and Geng (2023). The Sun dominates with a maximum deflection of $1.7513 \times 10^6 \mu\text{as}$, consistent with the historical $1.75''$ value from the 1919 solar eclipse. Among the planets, Jupiter contributes the largest signal with $1.66 \times 10^4 \mu\text{as}$, followed by Saturn at $5.98 \times 10^3 \mu\text{as}$. For the terrestrial planets, Earth and Venus yield $574 \mu\text{as}$ and $493 \mu\text{as}$, respectively. The Moon produces a deflection of $26 \mu\text{as}$, while large satellites such as Ganymede ($35 \mu\text{as}$) and Titan ($32 \mu\text{as}$) also reach the μas level. In the asteroid population, Ceres is the only object exceeding $1 \mu\text{as}$ ($1.22 \mu\text{as}$). These results demonstrate that in the microarcsecond regime, not only the Sun and planets but also large moons and a few asteroids must be included in precision modelling.

Second, the uncertainty analysis shows that the error budget of light deflection is almost entirely dominated by the measurement uncertainty of Newton's gravitational constant G . Using the CODATA 2018 recommended value, the relative uncertainty is $\sigma_G/G = 2.2 \times 10^{-5}$, whereas the uncertainties of planetary masses are smaller by 3–4 orders of magnitude. Consequently, improving the precision of light deflection predictions requires a more accurate determination of G , rather than refinements in planetary mass estimates.

In addition, the study of angular impact ranges confirms that the Sun nearly covers the

entire range, with an impact angle of 179.997° even at the $0.1 \mu\text{as}$ threshold. Jupiter has the strongest planetary contribution, ranging from 64° to 85° at the $1 \mu\text{as}$ threshold, while Saturn spans 12.6° to 15.4° . Although of low mass, the Moon produces a local influence of 6.7° at $1 \mu\text{as}$ due to its close proximity to Earth.

Finally, this work introduces and validates a dual-planet light deflection framework, where the combined influence of two planetary bodies is modeled through linear superposition. The results indicate that while the dominant contribution often comes from a single massive planet, secondary bodies can produce systematic shifts at the microarcsecond level. This highlights the necessity of incorporating dual-body effects into future SKA astrometric pipelines to avoid residual biases and further refine the determination of the gravitational constant G .

In summary, this work not only validates the consistency of gravitational light deflection theory with previous numerical studies but also highlights the dominant role of the gravitational constant G in limiting predictive accuracy. These findings provide theoretical and numerical support for the potential feasibility of constraining G through high-precision astronomical observations in the era of the Square Kilometre Array (SKA).

5.2 Limitation

This study also has several limitations. The analysis is based on the first-order light deflection formula, without including higher-order relativistic effects such as multi-body corrections or frame-dragging, which may become relevant at sub-microarcsecond precision. The celestial sample is limited to the Sun, planets, and a few major satellites and asteroids, while minor bodies were not systematically considered. In addition, the results rely entirely on the JPL DE440s ephemerides and CODATA values of G , without validation against real observational data. Finally, the numerical evaluation was performed at fixed epochs, and long-term observational effects or noise conditions were not addressed.

5.3 Future Work

In terms of data and observations, future studies could incorporate high-precision radio astronomical measurements (such as VLBI and the upcoming SKA) to test the reliability of the numerical simulations. Moreover, it would be valuable to explore the feasibility of constraining the gravitational constant G through direct comparison with observational results.

Finally, from an application perspective, long-term observational simulations under realistic noise conditions should be performed. This will help to evaluate the robustness of the model and assess the potential role of light deflection effects in future high-precision astrometry and deep-space navigation missions.

Bibliography

- [1] Zhaobo Wang. Gravitational constant from light deflections by solar system objects. UCL Research Essay, Scientific and Data Intensive Computing MSc, Department of Physics and Astronomy, 2025.
- [2] Jiahao Geng. The effect of light deflection by solar system objects on high-precision square kilometre array astrometry. Master's thesis, University College London, 2023. MSc Scientific and Data Intensive Computing.
- [3] Yingjie Li, Ye Xu, Shaibo Bian, ZeHao Lin, JingJing Li, DeJian Liu, and Chaojie Hao. The effect of light deflection by solar system objects on high-precision square kilometre array astrometry. *The Astrophysical Journal*, 938(1):58, October 2022.
- [4] L. Bernus, A. Hees, O. Minazzoli, Y. Dirian, D. Blas, A. Fienga, B. Lamine, M. Gastineau, and B. Christophe. Constraining the mass of the graviton with the planetary ephemeris inpop. *Physical Review Letters*, 123:161103, 2019.
- [5] Mariateresa Crosta. Astrometry in the 21st century: From hipparchus to einstein. *La Rivista del Nuovo Cimento*, 42(10):443–510, 2019. Published online 14 October 2019.
- [6] Peter J. Mohr, Barry N. Taylor, and David B. Newell. Codata recommended values of the fundamental physical constants: 2010. *Reviews of Modern Physics*, 84(4):1527–1605, 2012.
- [7] A. Bonaldi et al. Square kilometre array science data challenge 1: analysis and results. *Monthly Notices of the Royal Astronomical Society*, 500(3):3821–3837, 2021.
- [8] Robert Braun, Anna Bonaldi, Tyler Bourke, Evan Keane, and Jeff Wagg. Anticipated performance of the square kilometre array – phase 1 (ska1), 2019.
- [9] Chao Xue, Jian-Ping Liu, Qing Li, Jun-Fei Wu, Shan-Qing Yang, Qi Liu, Cheng-Gang Shao, Liang-Cheng Tu, Zhong-Kun Hu, and Jun Luo. Precision measurement of the newtonian gravitational constant. *National Science Review*, 7(12):1803–1817, 2020.

- [10] Øyvind Grøn and Sigbjørn Hervik. *Einstein's general theory of relativity: with modern applications in cosmology*. Springer Science & Business Media, 2007.
- [11] Clifford M. Will. The 1919 measurement of the deflection of light. *Classical and Quantum Gravity*, 32(12):124001, 2015.
- [12] Sergei M. Kopeikin. Testing the relativistic effect of the propagation of gravity by very long baseline interferometry. *The Astrophysical Journal*, 556(1):L1, July 2001.
- [13] M. J. Rioja and R. Dodson. Precise radio astrometry and new developments for the next generation of instruments. *The Astronomy and Astrophysics Review*, 28:6, 2020.
- [14] Christian Rothleitner and Stephan Schlamminger. Invited review article: Measurements of the newtonian constant of gravitation, g. *Review of Scientific Instruments*, 88(11), 2017.
- [15] Zhong-kun Hu, Qi Liu, and Jun Luo. Determination of the gravitational constant g. *Frontiers of Physics in China*, 1(4):449–457, 2006.
- [16] Axel Nothnagel. Very long baseline interferometry. In *Mathematische Geodäsie/Mathematical Geodesy: Handbuch der Geodäsie, herausgegeben von Willi Freeden und Reiner Rummel*, pages 1257–1314. Springer, 2020.
- [17] F. Malbet, C. Boehm, A. Krone-Martins, V. Lainey, L. Lindegren, M. Ramos-Lerate, A. Sozzetti, I. Tereno, and T. Zingales. Faint objects in motion: the new frontier of high precision astrometry. *Experimental Astronomy*, 51:845–886, 2021.
- [18] Congyuan Qu, Danhe Chen, Xiufeng Zhong, and Xin Lai. Multi-body dynamics-based design for jupiter' s natural satellite transfer mission. In *2024 2nd Asian Aerospace and Astronautics Conference (AAAC)*, pages 75–80. IEEE, 2024.
- [19] Eite Tiesinga, Peter J Mohr, David B Newell, and Barry N Taylor. Codata recommended values of the fundamental physical constants: 2018. *Journal of physical and chemical reference data*, 50(3), 2021.
- [20] Peter Mohr, David Newell, Barry Taylor, and Eite Tiesinga. Codata recommended values of the fundamental physical constants: 2022, 2024.
- [21] Amanda Weltman, P Bull, S Camera, K Kelley, H Padmanabhan, J Pritchard, Alvise Raccanelli, S Riemer-Sørensen, L Shao, S Andrianomena, et al. Fundamental physics with the square kilometre array. *Publications of the Astronomical Society of Australia*, 37:e002, 2020.

- [22] J McMullin, P Diamond, A McPherson, R Laing, P Dewdney, A Casson, L Stringhetti, N Rees, T Stevenson, M Lilley, et al. The square kilometre array project. In *Ground-based and airborne telescopes VIII*, volume 11445, pages 215–232. SPIE, 2020.
- [23] Zephyr Penoyre, Vasily Belokurov, N Wyn Evans, A Everall, and SE Koposov. Binary deviations from single object astrometry. *Monthly Notices of the Royal Astronomical Society*, 495(1):321–337, 2020.
- [24] Ryan S Park, William M Folkner, James G Williams, and Dale H Boggs. The jpl planetary and lunar ephemerides de440 and de441. *The Astronomical Journal*, 161(3):105, 2021.
- [25] Siwei Luo, Wei Yang, Shaolong Chen, and Furong Lin. Solar system dynamics with jet propulsion laboratory ephemeris. In *International Conference on Data and Information in Online*, pages 181–190. Springer, 2023.
- [26] Xu Lu, Tian-Ning Yang, and Yi Xie. Lunar time ephemeris lte440: User manual. *arXiv preprint arXiv:2506.19213*, 2025.
- [27] Boyan Kostadinov and Satyanand Singh. Discovering kepler’ s third law from planetary data. 2021.
- [28] Rodolfo G Cionco and Dmitry A Pavlov. Solar barycentric dynamics from a new solar-planetary ephemeris. *Astronomy & Astrophysics*, 615:A153, 2018.
- [29] Yi Su. *A New Introduction to Astronomy*. Huazhong University of Science and Technology Press, Wuhan, 2nd edition, February 2002.
- [30] T Troy McConaghy, Damon F Landau, Chit Hong Yam, and James M Longuski. Notable two-synodic-period earth-mars cycler. *Journal of Spacecraft and Rockets*, 43(2):456–465, 2006.